



**INSTITUT
POLYTECHNIQUE
DE PARIS**

M2 Report

**Field of Study: Turbulence Modeling, Data-Driven
Methods and Machine Learning**

Data Driven Turbulence Model for Transitional Aeroelastic Instabilities

Confidentiality Notice

Non-confidential report and publishable on Internet

**Author:
Pedro Morel Rosa**

**Host Organism Tutor:
Vincent Mons
Olivier Marquet**

Internship from 07/03/2022 to 05/08/2022

**Name of the host organism: ONERA
Address: 8 Rue des Vertugadins
Meudon, France**

Confidentiality Notice

This present document is not confidential. It can be communicated outside in paper format or distributed in electronic format.

Abstract

This work comparatively investigates different adjustments to the Spalart-Almaras turbulence model through corrective control parameters obtained by data-driven techniques. From a physical perspective, the main objective is to obtain an accurate description of the *laminar separation flutter* phenomenon, which does not present satisfactory results when simulated using classical turbulence methods and models. The complexity of the phenomenon and its highly localized character are used in order to promote a comparative study of configurations that differ in the type of modeling and nature of the data used for correction (parietal data or full field data). This investigation shows that it is possible to obtain a corrected model for Spalart-Almaras that accurately provides the aerodynamic forces intrinsic to the phenomenon. However, the data choices and the nature of the correction are not trivial and different advantages and shortcomings are explored until an optimal configuration is obtained. To this end, adjunct sensitivity analyzes are constantly used, in order to provide guidelines in terms of physical understanding of the correctness and effectiveness of the models obtained.

Keywords: turbulence modeling, computational methods, optimization, field inversion, data assimilation, machine learning, neural networks.

Résumé

Ce travail étudie de manière comparative différents ajustements du modèle de turbulence Spalart-Almaras grâce à des paramètres de contrôle correctifs obtenus par des techniques basées sur des données. D'un point de vue physique, l'objectif principal est d'obtenir une description précise du phénomène de *laminar separation flutter*, qui ne présente pas de résultats satisfaisants quand simulé à l'aide de méthodes et de modèles de turbulence classiques. La complexité du phénomène et son caractère très localisé sont mis à profit pour favoriser une étude comparative de configurations qui diffèrent par le type de modélisation et la nature des données utilisées pour la correction (données pariétales ou données plein champ). Cette investigation montre qu'il est possible d'obtenir un modèle corrigé pour Spalart-Almaras qui fournit avec précision les forces aérodynamiques intrinsèques au phénomène. Cependant, les choix de données et la nature de la correction ne sont pas triviales, et différents avantages et inconvénients sont explorés jusqu'à l'obtention d'une configuration optimale. À cette fin, des analyses de sensibilité complémentaires sont constamment utilisées, afin de fournir des lignes directrices en termes de compréhension physique de l'exactitude et de l'efficacité des modèles obtenus.

Mots-clés: modélisation de la turbulence, méthodes numériques, optimisation, field inversion, assimilation de données, apprentissage automatique, réseaux de neurones.

Acknowledgements

O presente é tão grande, não nos afastemos. Não nos afastemos muito, vamos de mãos dadas

The present is so large, let's not stray far. Let's stay together and go hand in hand

Carlos Drummond de Andrade, *Mãos Dadas*

This work, as well as my studies in Brazil and France, would never be possible without the people I love, whose unconditional support is indifferent to distance.

I give heartfelt thanks to everyone in my family, those who live and stand by my side, and those who are no longer there but whose teachings and memories I will carry forever.

I also thank my friends in Rio and Paris, without whom daily life would be less easy. To everyone, thank you, merci, obrigado.

I express my gratitude to my research supervisors, Vincent Mons, Pedro Volpiani and Olivier Marquet, thank you for the opportunity and mentoring.

To every teacher I have had in life, since the very beginning of my education until now, I can not thank you enough.

Dedicated to my grandfather,

Contents

Confidentiality Notice	2
	3
Acknowledgements	4
Contents	6
Introduction	8
1 Laminar Separation Flutter	9
1.1 Introduction	9
1.2 Types of Instabilities	9
1.3 Transitional Flow Regime	10
2 Direct Numerical Simulation	13
2.1 Introduction	13
2.2 Properties Analysis	14
2.2.1 Direct Properties	14
2.2.2 Processed Properties	16
2.3 Aerodynamic Coefficients	18
3 Classic Modeling Framework	20
3.1 RANS Equations	20
3.1.1 Introduction	20
3.1.2 RANS Derivation	21
3.1.3 Boussinesq Hypothesis	21
3.2 Spalart-Allmaras Model	22
3.2.1 Modified Eddy-Viscosity	22
3.2.2 Turbulence Equation	23
3.3 Transition Model	24
4 Numerical Implementation	26
4.1 Introduction	26
4.2 Methodology	26
4.2.1 Numerical Domain	26
4.2.2 Weak Formulation	27
4.2.3 Mesh Generation	28
4.2.4 Finite Element Method	30
4.3 Preliminary Results	30

5 Data Assimilation	33
5.1 Introduction	33
5.2 Methodology	34
5.2.1 Modified Spalart-Allmaras Modelling	35
5.2.2 Variational Data Assimilation	36
5.2.3 Tools and Techniques	38
5.3 Results: Scenario I	40
5.3.1 Motivation	40
5.3.2 Analysis for $\alpha = 2^\circ$	41
5.3.3 Analysis for $\alpha = 1$	44
5.3.4 Analysis for Every α	45
5.3.5 Broader Strategies	47
5.4 Results: Scenario II	48
5.4.1 Motivation	48
5.4.2 Field Data	48
5.4.3 Additional Forcing	50
5.5 Conclusion	52
 Conclusion	 53
 Bibliography	 54
 List of Tables	 57
 List of Figures	 58

Introduction

The understanding of aeroelastic phenomena is of paramount importance for the progress and evolution of aircraft technology. This branch of aerodynamics studies particularly the interaction between aerodynamic forces and the response of a structure subjected to a certain flow. Advances in this area made it possible to prevent disasters and failures caused by aerodynamic instabilities, such as flutter. However, it remains with complex open questions, especially for Reynolds regimes little explored by classical aviation. Notably, a new type of instability was observed by Poirel et al. [1] in a transitional Reynolds regime ($Re\ 10^4 - 10^5$) for a NACA0012 airfoil at low incidences. It is characterized by a self-sustained pitch oscillation, and caused by the detachment of the initially laminar boundary layer, followed by its transition and subsequent reattachment. This phenomenon is called laminar separation flutter. This subject is covered in more detail in Chapter 1.

This work, however, does not aim to bring contributions and results from a physical point of view, as has been brilliantly done in other articles ([2] [3] [4]). But instead, it takes advantage of the complexity of this phenomenon to contribute in the area of turbulence modeling, pushing the limits of well established models. The relevance of this study is reiterated mainly in view of the inability to correctly predict this phenomenon using classical tools, like RANS simulations complemented by low-cost turbulence models, such as Spalart-Allmaras [3].

With this in mind, this work proposes, at first, a corrective term for the turbulence model. This correction is achieved by the data assimilation (or field inversion) technique, which takes advantage of high-fidelity data by solving an optimization problem. Chapter 2 is dedicated to a presentation and analysis of the high-fidelity data used in this work, obtained through a DNS simulation. Consecutively, the classical modeling framework used in this work will be discussed in Chapter 3, consisting of the RANS modeling with the Spalart-Allmaras turbulence equation; alongside with the BCM transition model. In order to understand the numerical tools and methods used to simulate the aforementioned mathematical framework; Chapter 4 will deal with the numerical implementation, supported by the Finite Element Method. Additionally, a direct comparison will be made between DNS and RANS simulation.

Finally, Chapter 5 will formally address the data assimilation technique. Several studies have already proposed similar models [4] [5], introducing a multiplicative correction to the production or destruction terms in the turbulence equation. However, few of them carried discussions about ideal modeling choices. Among them, what should be the form of this corrective term? And how does it influence the performance of correction? Additionally, different physical data can be used as a reference for the optimization problem. How does data influence prediction capabilities? These answers are given in depth through adjoint sensitivity analyses, in addition to a thorough comparative study of the results. A rigorous technical presentation and discussion of results is carried in this Chapter.

Chapter 1

Laminar Separation Flutter

“Setbacks and disasters are negative virtues.”

Alberto Santos Dumont

This chapter aims to objectively discuss the physical phenomenon that underpins this work. Given its complexity and highly nonlinear nature, laminar separation flutter is an aeroelastic instability discovered in recent years. In order to present it satisfactorily, it is necessary to contextualize aeroelasticity studies. Next, a brief discussion of aeroelastic instabilities will be carried out, followed by pertinent comments about the nature of the transitional Reynolds regime. Finally, the laminar separation flutter will be presented; along with recent research advances.

1.1 Introduction

Not long after the first officially observed flight, carried out in Paris by Brazilian engineer Alberto Santos Dumont, an effervescent era of evolution of aircraft designs began. The desired advances were clear: more maneuverability, rate of climb and speed. However, many of these improvements were made at the expense of a solid structural construction, making aeroelastic instabilities more likely to occur. For some years, there were no explanations for some of the failures seen in the aviation world, and much progress was made in an ad-hoc, trial and error manner.

The solution to these failures came only in the 1930s, with the pioneering works of [6], [7] and [8]. The paradigm shift is due to the understanding that aeroelastic phenomena are an interaction between aerodynamic, elastic and inertial forces of a flow field acting on a structure. Instabilities arise from a feedback process: flexible structures undergo deformations caused by aerodynamic forces, and in turn, these deformations change the aerodynamic load distribution; resulting in an ongoing interplay.

More holistically, a broad scope of domains makes use of fluid-structure interaction; from the study of aneurysms with blood flow modeling to the study of the stability of bridges in the face of winds [ref IFS].

1.2 Types of Instabilites

There are two categories of aerodynamic instabilities: dynamic instabilities and static instabilities, defined respectively based on the oscillatory behavior, or not, of the structure. Both are illustrated in Figure 1.1, compared to a rigid wing mounted on a torsion spring.

One classic example of static instability is the divergence instability. This phenomenon arises whenever the aerodynamic moment exerted by the flow onto the wing cannot be counterbalanced by the elastic stiffness of the structure, resulting in a non-oscillatory deviation of the wing incidence from its equilibrium position.

Among the different types of dynamic aeroelastic instability, flutter is the most classic example. This phenomenon occurs when the total damping of the dynamics is negative, resulting in scenarios of amplification of certain perturbations. Under a linear approach, one can determine the "critical reduced speed" of an aircraft, which corresponds to zero net damping, and therefore, the onset of flutter.

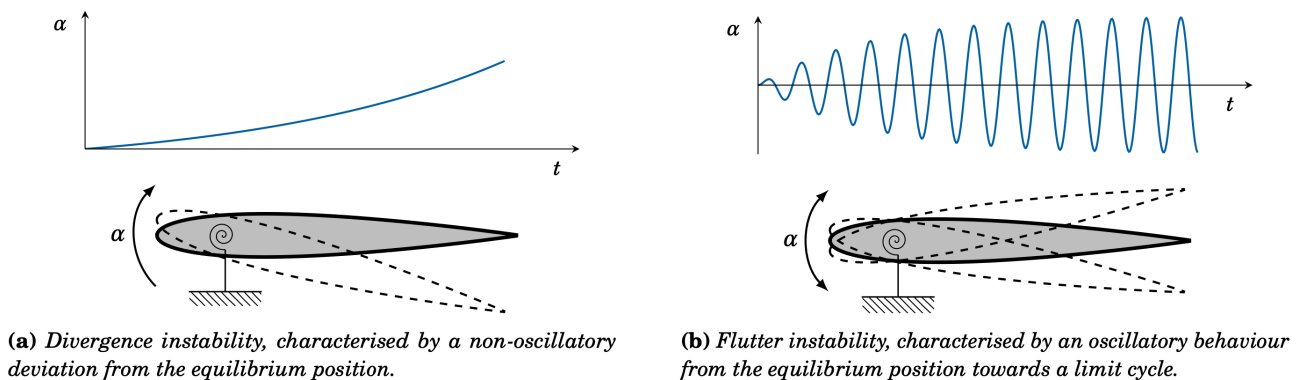


Figure 1.1: Static instability and dynamic instability, respectively. Sabino et al. [2]

Furthermore, there are several types of flutter, among which we can mention the coupled-mode flutter, transonic flutter, stall flutter and the laminar separation flutter; which is of most interest for this work, and the least understood. In order to explain it better, one has to understand the physical context responsible for its emergence: transitional flows.

1.3 Transitional Flow Regime

For high Reynolds regimes, turbulent flow is readily achieved from the first contact with the leading edge of the wing. This regime is characteristic of commercial flights, and leads to the attachment of the turbulent boundary layer to the wing surface for a relatively large scope of angles of attack. However, for aircraft with smaller dimensions such as drones and gliders the Reynolds number is situated in a transitional regime $Re \in (10^4, 10^6)$, and the transition does not promptly occur at the leading edge of the wing. Given this, there is a coexistence of laminar, transitional and turbulent regions; giving rise to nonlinear dynamics, and so, complex viscous phenomena.

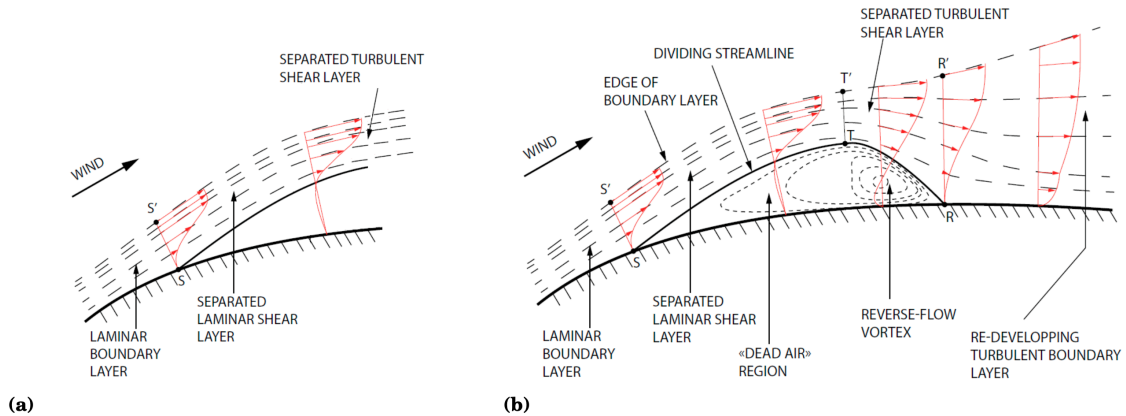


Figure 1.2: Schematic illustration of a two-dimensional laminar boundary layer separation and of a laminar separation bubble, respectively. Busquet et al. [9]

In addition, the post-separation laminar flow becomes highly sensitive to perturbations, and therefore susceptible to transition to turbulence. With that in mind, two scenarios can occur: the flow remains separated by the entire remaining surface of the wing; resulting in a wake downstream from the trailing edge. In general, this scenario presents higher drag and possibly lift breakdown. On the other hand, if adverse pressure gradients are sufficiently large, reattachment will occur; producing a recirculation zone commonly known as laminar separation bubble (LSB). Inside the bubble the flow may be circulating and the velocity near the airfoil surface may even be the opposite direction of velocity the outer flow. There is almost no energy exchange with the outer flow, which makes the LSB quite stable.

Classically, the laminar separation bubbles were classified into two types: short and long bubbles [10]. Short bubbles (Left Fig. 1.3) were defined as possessing a bubble length approximately 10^2 times the displacement thickness of the boundary layer at the separation point, corresponding only to a few percent points of the chord. On the other hand, long bubbles (Right Fig. 1.3) were defined as having a length of order 10^4 times the displacement thickness of the boundary layer at the separation point, corresponding to more than 20% of the entire airfoil.

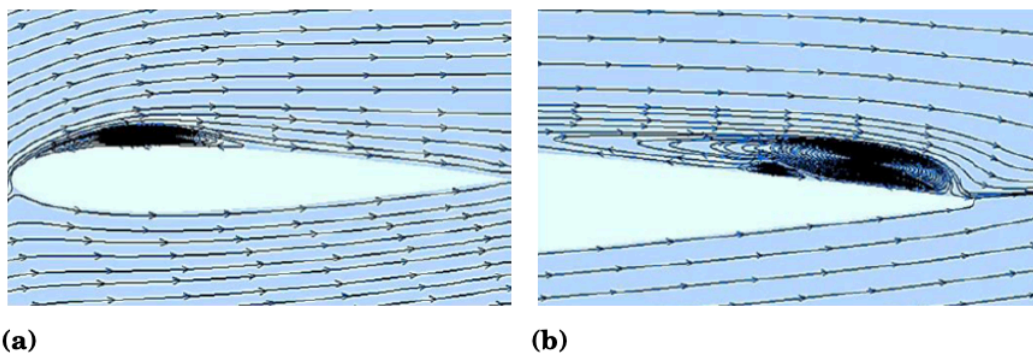


Figure 1.3: A short laminar separation bubble and a long laminar separation bubble, respectively. Xia et al. [11]

The comments and particularities of the transient Reynolds regime discussed here were made for a fixed airfoil case, in which the structure dynamics is not taken into account. Now, still in this physical context, an investigation will be carried out from the perspective of fluid-structure

instabilities. The phenomenon that interests this work is the laminar separation flutter, in which the LSB and the negative aerodynamic moment are linked to structure oscillations.

As previously mentioned, the complexity of this phenomenon is manifested through a non-linear behavior that is difficult to predict, especially for aerodynamic efforts. Muller et al. [12] were the first to report this fact, denoting that for angles of attack in the range $0^\circ < \alpha < 3^\circ$, the lift coefficient is negative. This study was done for the symmetric NACA66₃-018 airfoil, and this phenomenon is observed particularly at $Re = 130000$. Below and above this Reynolds number, no negative lift is observed. The same observations were described recently for a NACA0012 airfoil by Ohatake et al [13]. They observed this phenomenon for Reynolds numbers between $Re = 25000$ and 70000 , and detected the presence of a low drag regime for angle of attacks in the range of $-11^\circ < \alpha < 11^\circ$.

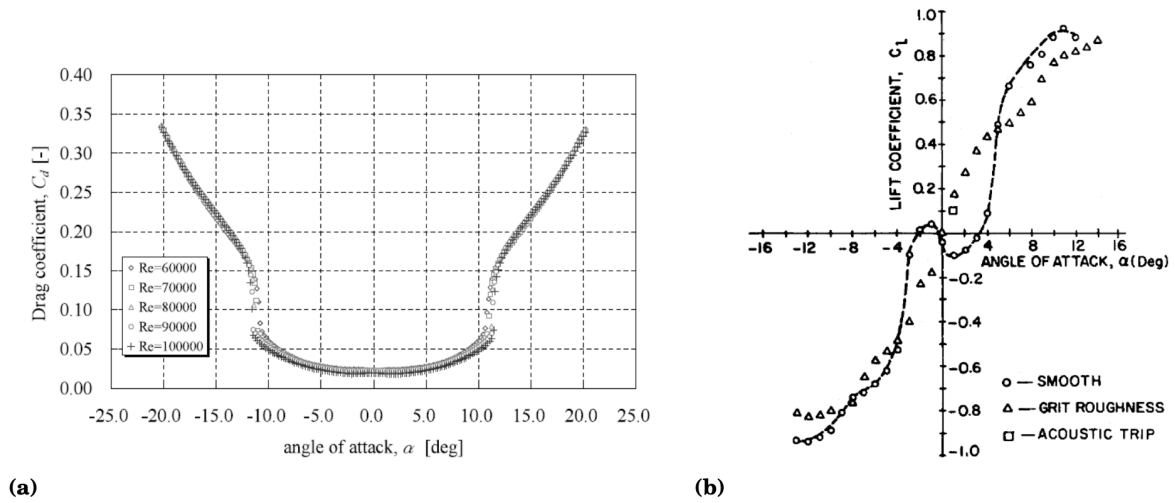


Figure 1.4: On the left, evolution of the time-averaged drag coefficient with the angle of attack for different Reynolds numbers, from the experiments of Ohtake et al. [13]. On the right, evolution of the time-averaged lift coefficient with the angle of attack for $Re = 130000$, from the experiments of Mueller et al. [12]

Chapter 2

Direct Numerical Simulation

This chapter is dedicated to the presentation and analysis of high-fidelity data that will serve as a foundation for the techniques that this work aims to study. At first, the concept of DNS (Direct Numerical Simulation) and the nature of this type of numerical solution will be presented. This will be followed by a brief discussion regarding the physical context of this results and how it relates to the concepts presented in Chapter 1. Finally, an extensive analysis of properties that can be obtained directly and indirectly from the data will be carried out. This step is of fundamental importance for an adequate understanding of the phenomenon and the nature of the data; and which will guide decisions and considerations within the scope of modeling.

2.1 Introduction

The Navier-Stokes equations are a set of partial differential equations which describe the motion of viscous fluid substances. For incompressible and Newtonian fluids, the conservation of mass and conservation of momentum equations can be respectively stated as

$$\nabla \cdot \mathbf{u} = 0 \quad (2.1)$$

$$\frac{\partial(\mathbf{u})}{\partial t} + (\mathbf{u} \cdot \nabla)\mathbf{u} = -\frac{1}{\rho}\nabla p + \nu\Delta\mathbf{u} \quad (2.2)$$

These equations are considered to be the most robust mathematical representation for the description of fluid dynamics, and for a wide range of applications, they are used for an accurate description of phenomena under different physical conditions and geometries.

In 1970, mathematician Steven Orszag presented in his article "Analytical Theories of Turbulence" two main ways - so far - to obtain theoretical results regarding turbulence [14]. The first was through theories of turbulence, which sought to ground a phenomenological understanding of problems that presented turbulence. Alternatively, one could *directly* solve Navier-Stokes via numerical simulation. The term DNS has been used recurrently since then.

However, one may encounter several adversities of numerical nature when opting for this type of solution. Notably, considering the classical theory of turbulence, it is known that the energy of a flow dissipates only in spatial dimensions that lie on the Kolmogorov scale

$$\eta = \left(\frac{\nu^3}{\varepsilon}\right)^{\frac{1}{4}}$$

where ν is the kinematic viscosity and ε is the rate of kinetic energy dissipation. Then, taking into consideration the definition of the Reynolds number and the properties used in defining the Kolmogorov scale, one can prove that this scale exponentially depends on the Reynolds number.

This means that as the flow becomes more turbulent, the spatial resolution of the dissipation becomes substantially lower. And given the highly nonlinear nature of the Navier-Stokes equations, this poses a problem. If these scales are not solved accurately at the numerical level, the nonlinear character of the equation will exponentially increase the errors; can lead to solutions that diverge substantially from physics.

The purpose of this brief discussion regarding the nature of a direct numerical simulation is to denote the fact that this operation can demand high computational power and time. It is for this reason that turbulence models were developed as alternatives to DNS. Among them, the Spalart-Allmaras model will be discussed in Chapter 4.

Fortunately, for this work, data from a direct numerical simulation were provided by Sabino [2], who studied in depth the stability of the phenomenon of laminar separation flutter through theoretical and numerical tools. Given the nature of baseflow, these variables provide a qualitative understanding of the physical magnitudes of the problem. Notably, U , V , W and P convey the average dynamics of the phenomenon in equilibrium. The remaining variables uu , vv , ww , uv , uw and vw denote fluctuations in velocity that the physical context presents. These results were obtained for 5 angles of attack: 0° , 0.5° , 1° , 1.5° and 2° ; all at $Re = 50000$ for a NACA0012 profile.

2.2 Properties Analysis

2.2.1 Direct Properties

In this first moment, analyzes based on direct visualizations of the quantities obtained by DNS will be presented. This discussion will reinforce qualitative results obtained in recent years regarding the Laminar Separation Flutter.

We start by showing the horizontal velocity of the baseflow around the NACA0012 airfoil REF-FIG. The loss of symmetry is easily noticed as the angle of attack increases; as well as the advance of the boundary layer detachment point in the extrados.

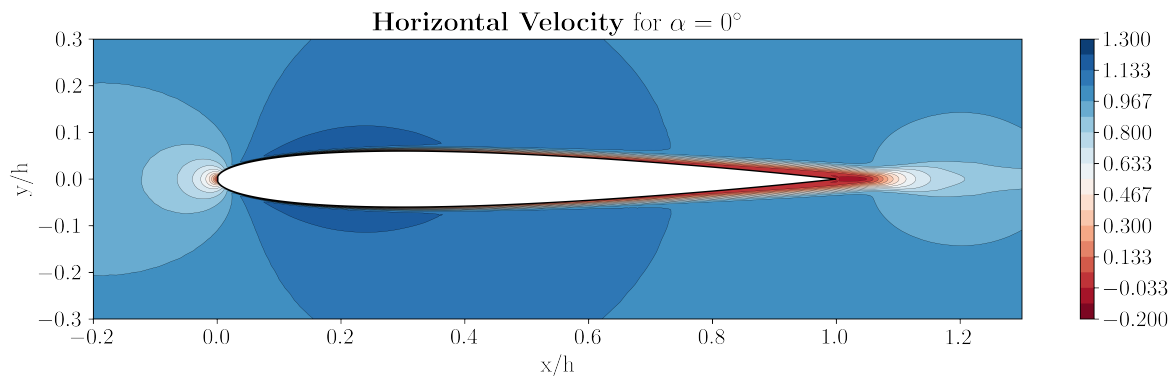


Figure 2.1: Horizontal velocity comparison angle of attack $\alpha = 0^\circ$.

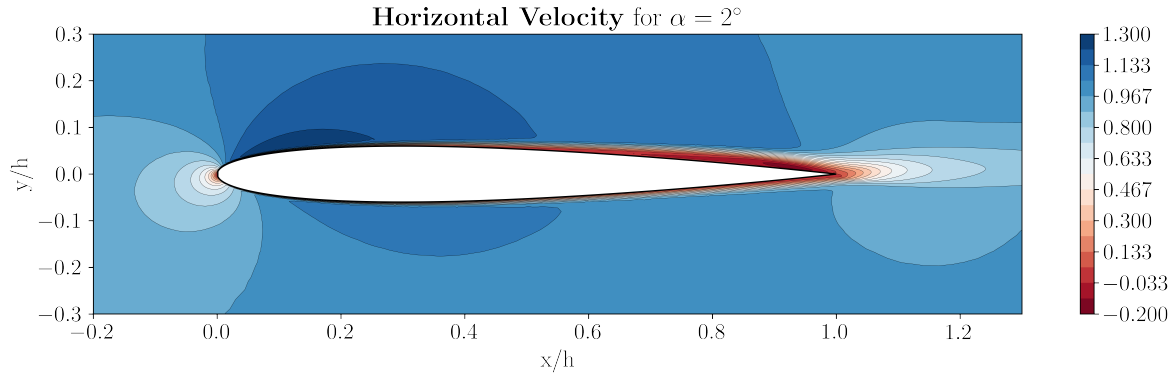


Figure 2.2: Horizontal velocity comparison angle of attack $\alpha = 2^\circ$.

On a more cautious analysis of the last image of Fig. 2.2, one can easily perceive the laminar separation bubble formed in the extrados, close to the trailing edge (Fig. 2.3). The scales for this visualization were adapted in order to facilitate the identification of the region from which the horizontal velocity becomes adverse.

In particular, in this region, one can denote the existence of a thin layer of positive velocity amidst the adverse velocity field. It accurately represents the contour of the laminar separation bubble; containing within it a recirculation zone represented by shades of more intense red.

Through visualizations of the same nature, it is easy to see that this recirculation zone begins to form from an attack incidence of 1° . This fact is of substantial relevance, as it explains the pertinent intricacies of the dynamics for an angle between 0° and 1° ; and between 1° and 2° .

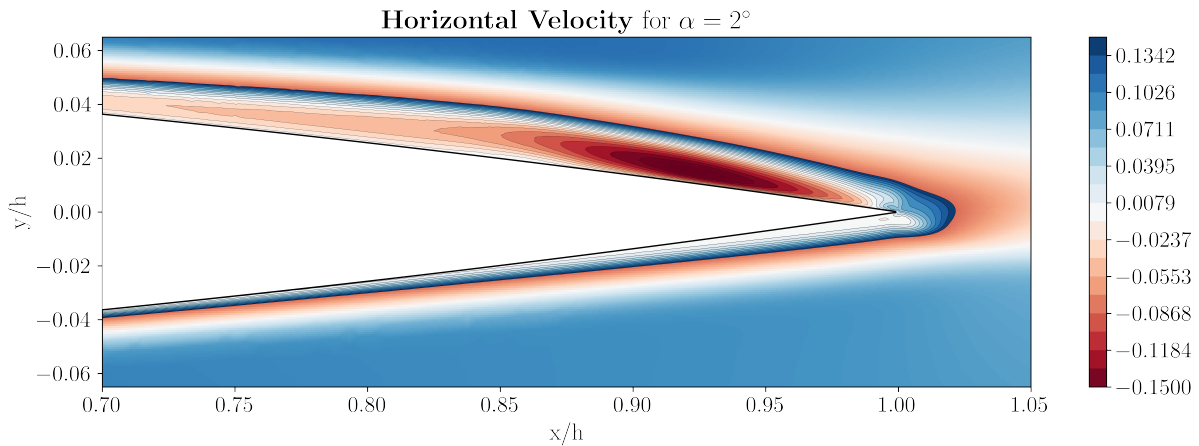


Figure 2.3: Horizontal velocity for $\alpha = 2^\circ$, denoting the Laminar Separation Bubble.

Finally, we can check the evolution of the perturbation velocity term on the z-axis (Fig. 2.4). This physical quantity serves as a metric of the three-dimensional order variations that are ignored when analyzing only the superposition of this dynamics in 2D. Based on this, it can be concluded that as we approach $\alpha = 2^\circ$, the phenomenon presents a more intricate dynamics in different planes along the z-axis.

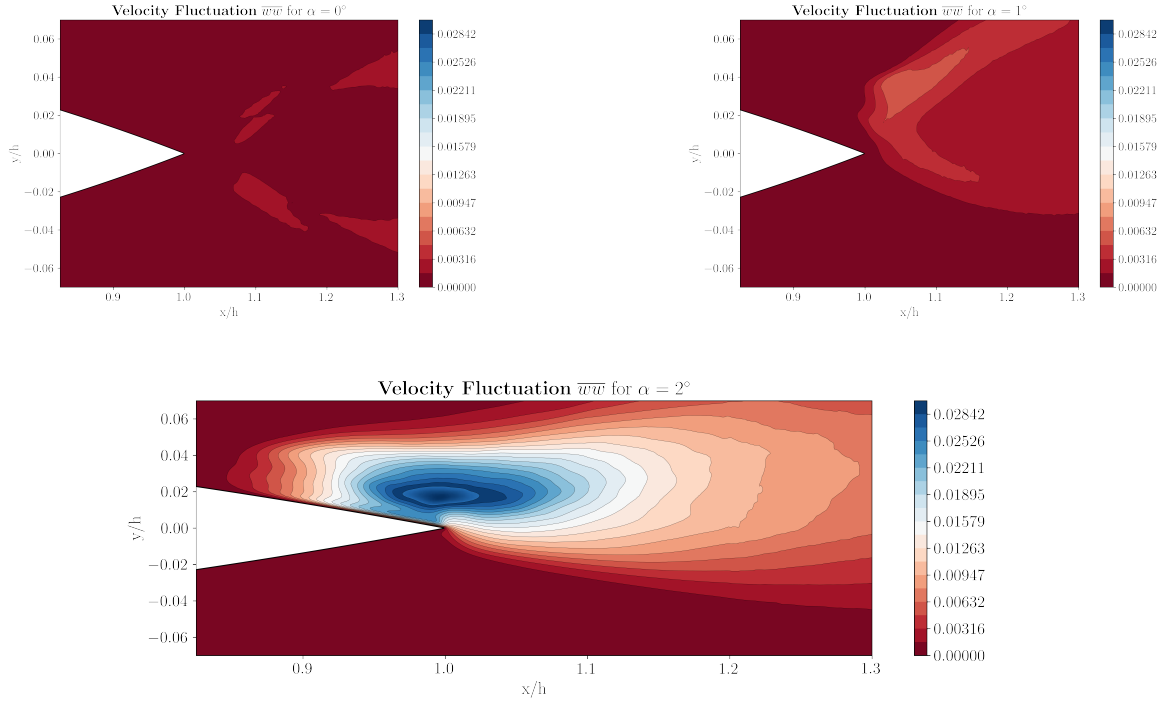


Figure 2.4: Fluctuation term in z direction comparison for different angles.

2.2.2 Processed Properties

In addition to the properties presented above, there are other physical quantities that are of interest for this work and that will help to guide the aspects more related to modeling; that will be presented in the following chapters.

Along these lines, one can check the validity of Boussinesq's hypothesis; which serves as the basis for numerous RANS models. In essence, the Boussinesq hypothesis major claim is that the main axis of the Reynolds stresses coincides with those of the average strain. This allows the Reynolds stress tensor to be modeled analogously to the classical stress tensor; and a turbulent viscosity variable is introduced.

$$\overline{u'_i u'_j} = 2\nu_t S_{ij} - \frac{2}{3}k\delta_{ij}$$

Where ν_t is the turbulent viscosity, k is the turbulent kinetic energy and δ_{ij} is the Kronecker delta. Details pertinent to RANS modeling will be formally presented in Chapter 3.

Given this definition, Schmidt et al. [15] introduced an indicator defined through the inner product between the traceless stress tensor (also called the anisotropic stress tensor) $\mathbf{R} = \overline{u'_i u'_j} - \frac{2}{3}k\delta_{ij}$ and the mean strain rate tensor \mathbf{S}

$$\rho_{RS} = \frac{|\mathbf{R} : \mathbf{S}|}{\|\mathbf{R}\| \|\mathbf{S}\|} \quad (2.3)$$

This indicator measures the proportionality between these two tensors and is analogous to the cosine of the angle between vectors. The metric varies between 0 and 1, and if $\rho_{RS} = 1$, then Boussinesq's approximation is fully respected. Furthermore, Schmidt et al. [15] established (through geometrical reasoning) that if $\rho_{RS} > 0.86$, then it would make sense to use a linear eddy-viscosity approximation.

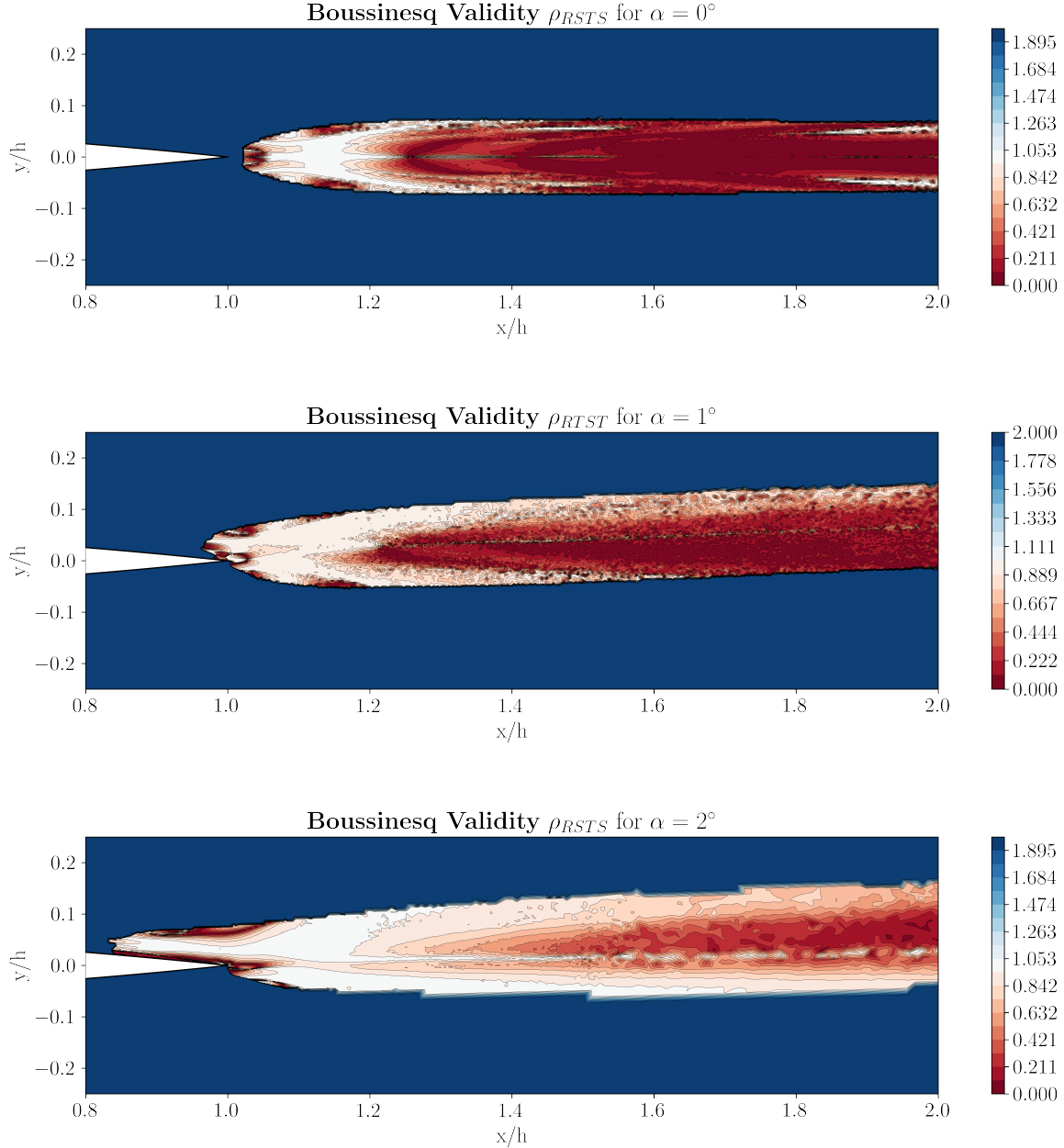


Figure 2.5: Boussinesq validity analysis for different angles of attack.

In view of these results, it is clear that the linear turbulent viscosity framework is sustained in the trailing edge region immediately after the profile. This fact surprisingly holds even for angles of attack greater than 1° , for which the laminar separation bubble is already formed. On the other hand, as we move further downstream from the profile, Boussinesq's hypothesis loses its validity. This discussion is of paramount importance, since this work aims to remain within a framework of modeling supported by Boussinesq's hypothesis.

Additionally, one can calculate the turbulence production term using the quantities provided by DNS. This physical quantity is quite relevant since it will be of absolute importance to understand the magnitude and spatial distribution of the turbulent aspects in the phenomenon.

$$\text{Production} = -\overline{uu} \frac{\partial U}{\partial x} - \overline{uv} \left(\frac{\partial V}{\partial x} + \frac{\partial U}{\partial y} \right) - \overline{vv} \frac{\partial V}{\partial y}$$

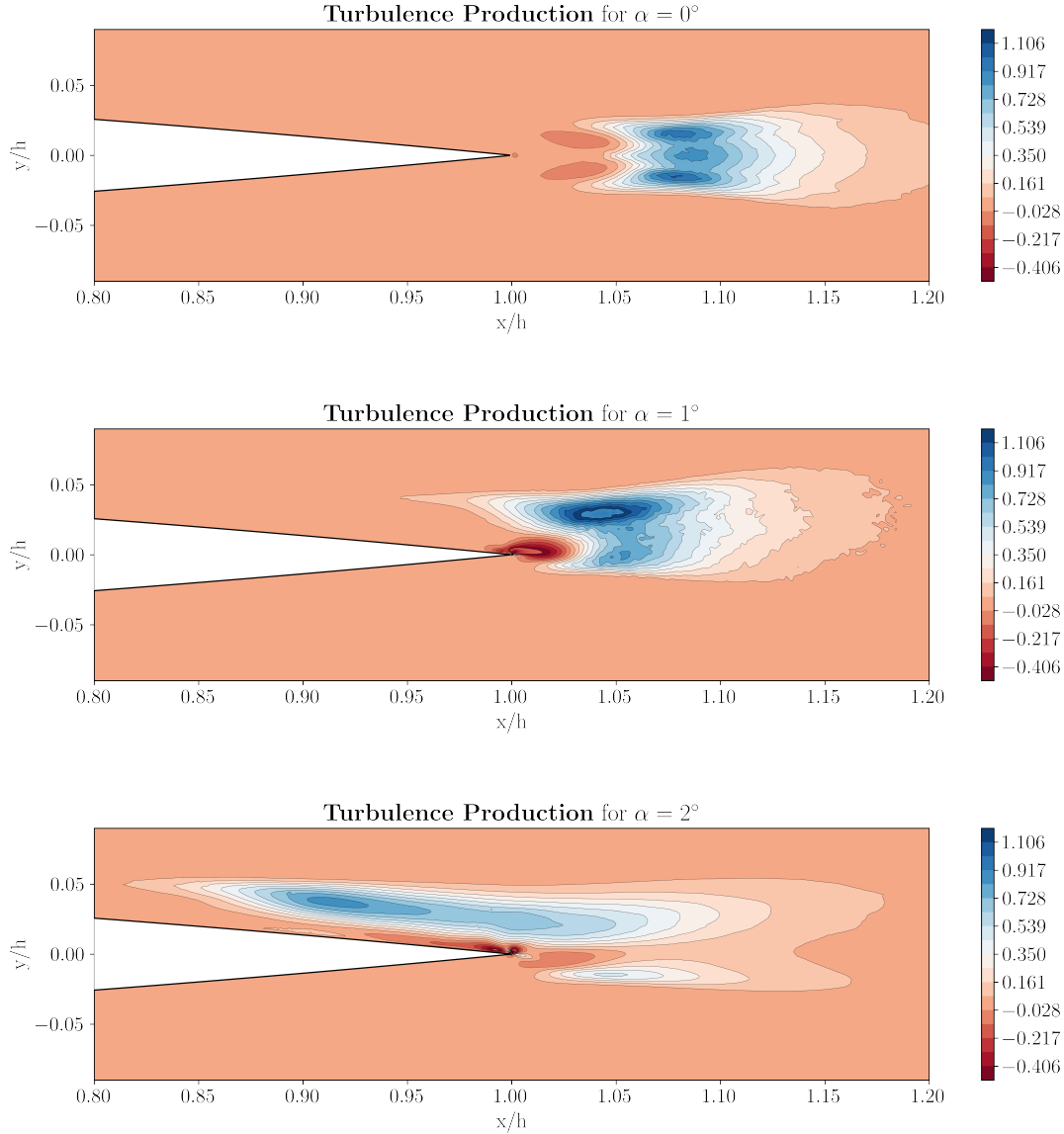


Figure 2.6: Turbulence production for different angles of attack.

And therefore, it is possible to expect that the chosen turbulence model will intervene in the regions shown in Fig. 2.6. It is reinforced that, as the angle of attack increases, a region of high dynamic complexity is formed near the trailing edge of the extrados.

2.3 Aerodynamic Coefficients

A final analysis that can be easily obtained using DNS data is within the scope of the aerodynamic efforts acting on the NACA0012 airfoil. In this context, the pressure coefficients C_p , skin friction C_f and moment coefficients C_m will be analyzed.

Initially, we show through the variation of the global efforts that, in fact, the complexity of the phenomenon is also translated in the aerodynamic forces that act on the profile. Notably, one should remark the highly nonlinear aspect linked to the variation of forces as we vary the angle of attack. This is also reinforced by qualitative factors, since the global lift remains negative until $\alpha = 1^\circ$ and

the global acting moment changes from negative to positive for an angle of attack between $\alpha = 1.5^\circ$ and $\alpha = 2^\circ$

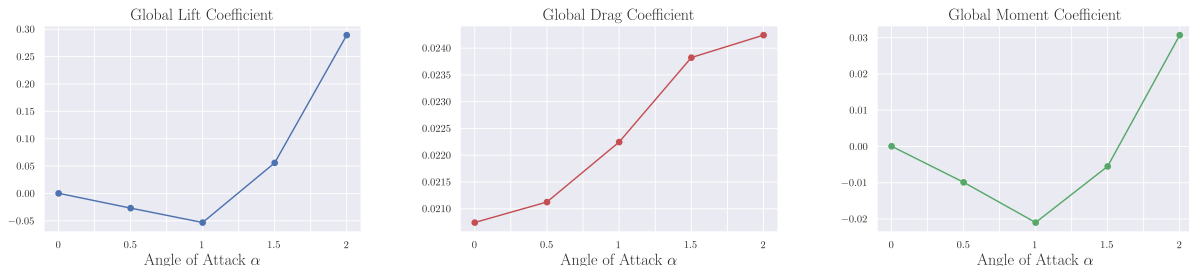


Figure 2.7: Global aerodynamic efforts for different angles of attack

Complementing this analysis, it is also possible to study the local influence of the laminar separation bubble on the airfoil. One quantity that best depicts these effects is the skin friction coefficient for the extrados. It can be clearly seen that for the incidence angles 1.5° and 2° , the value of C_f is negative precisely where we expect to find the LSB.

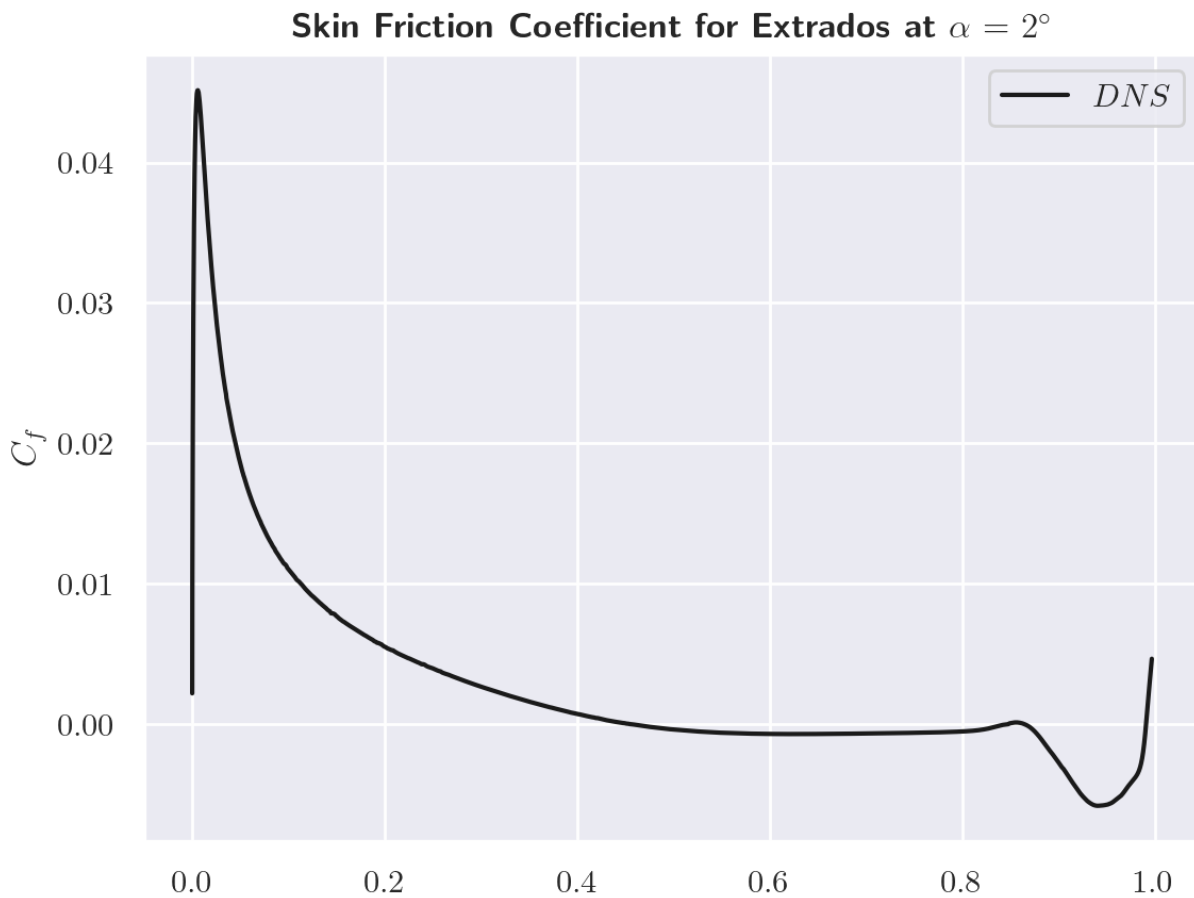


Figure 2.8: Skin Friction Coefficient at extrados for $\alpha = 2^\circ$

Chapter 3

Classic Modeling Framework

This chapter is devoted to formally presenting the modeling framework that will be studied in this work. At first, the averaging process and the Reynolds decomposition of the Navier-Stokes equations will be discussed; in addition to the paradigms linked to RANS modeling. Next, the Spalart-Allmaras turbulence model will be discussed in depth. This step is of crucial importance, since this work aims to obtain corrected Spalart-Allmaras models; therefore a robust understanding of the physical significance of each term in the model is indispensable. Finally, a discussion will be carried out about the role of transition models, which act in a complementary way and correct several deficiencies of classical RANS modeling in transition regimes.

3.1 RANS Equations

3.1.1 Introduction

As discussed in the previous chapter, Claude-Louis Navier (1785-1836) and George G. Stokes (1819-1903) formulated the fundamental mathematical framework for the description of Newtonian fluid flows. Despite the generality of the Navier-Stokes equations (2.1, 2.2) the diversity of scales present even today limits, in some cases, the direct numerical simulation of turbulent flows. Osborne Reynolds (1842-1912), however, provided a viable alternative to the classic solution. Realizing that the properties of turbulent flows can be described by superposing a fluctuating term to an average value, Reynolds suggests that the fields present in the governing equations be divided into average and fluctuating or turbulent components [16].

The formal result of this procedure is, of course, a new equation in which the turbulent field effects are isolated from the mean flow descriptive terms. Despite being attractive, this solution strategy poses a difficult obstacle: its application leads to the emergence of new dynamic variables. In this way, the modeling of the properties of turbulent flows in mean and stochastic components give rise to a number of independent dynamic variables greater than the number of available governing equations. The Reynolds strategy then results in a mathematically indeterminate problem, which is usually referred to as the “closing” problem. In a rigorous procedure, manipulating algebraic applications applied to the Navier-Stokes equations provides additional equations, which, in turn, present new higher-order unknowns. Such behavior is typically observed in nonlinear stochastic systems.

From this point of view, a turbulent velocity field decomposes into:

$$\mathbf{u}(\mathbf{x}, t) = \bar{\mathbf{u}}(\mathbf{x}) + \mathbf{u}'(\mathbf{x}, t)$$

where $\bar{\mathbf{u}}(\mathbf{x})$ is the average velocity (statistically stationary) and $\mathbf{u}'(\mathbf{x}, t)$ the fluctuating component.

The decomposition of Reynolds fields represents a way to introduce a statistical formulation for the description of the dynamics of turbulent flows, thus enabling its numerical modeling. However, as in all statistical descriptions, there is, necessarily, a loss of potential information important when adopting a restricted number of parameters.

3.1.2 RANS Derivation

Given the definitions discussed above, one can start the process of decomposing and averaging through the conservation of mass equation:

$$\frac{\partial u_i}{\partial x_i} = 0 \longrightarrow \frac{\partial(\overline{u_i + u'_i})}{\partial x_i} = 0 \longrightarrow \frac{\partial u_i}{\partial x_i} = 0 \quad (3.1)$$

In the above operations, the mean value of the spatial derivative of a quantity was assumed to be equal to the spatial derivative of the mean value of that same quantity. Which yields equation (3.1). The Navier-Stokes equation can therefore be rewritten using the chain rule in the second term on the left side of Eq. (2.2):

$$u_j \frac{\partial u_i}{\partial x_j} = \frac{\partial u_i u_j}{\partial x_j} - u_i \frac{\partial u_j}{\partial x_j} \quad (3.2)$$

where the second term on the right hand side is zero by the continuity equation. Using the above equality and taking the time average of the Navier-Stokes equation, one obtains:

$$\frac{\partial \overline{u_i}}{\partial t} + \frac{\partial \overline{u_i u_j}}{\partial x_j} = \frac{\partial \overline{\sigma_{ij}}}{\partial x_j} \quad (3.3)$$

Since the mean of $u_i(x, t)$ is statistically stationary, the first term on the left side of the last equation is zero. Taking into account now the Reynolds decomposition, and the reapplication of the averaging operator in Eq. (3.3):

$$\frac{\partial \overline{\rho u_i u_j}}{\partial x_j} = \frac{\partial}{\partial x_j} \left[\rho(\overline{u_i u_j} + \overline{u'_i u'_j}) \right] \quad (3.4)$$

and in turn, back in Eq. (3.1), we finally have the Navier-Stokes equations written in terms of the decomposition of Reynolds fields:

$$\rho \overline{u_j} \frac{\partial \overline{u_i}}{\partial x_j} = \frac{\partial}{\partial x_j} \left[\overline{\sigma_{ij}} - \rho \overline{u'_i u'_j} \right] \quad (3.5)$$

Equations (3.5) are usually called Reynolds Averaged Navier-Stokes equations (RANS). It is also observed they present exactly the same composition as the Navier-Stokes equation for laminar and stationary flows, Eq. (2.2), with the exception of the last term on the right hand side, which represents the turbulent contribution to the mean flow.

3.1.3 Boussinesq Hypothesis

As shown, the time-averaged deduction of the governing equations introduces new unknown terms, containing velocity fluctuation products $-u'_i u'_j$. These terms represent momentum fluxes that act as additional stresses in the flow, thus being called “turbulent stresses” or “Reynolds stresses”.

The first model for the mathematical description of turbulent stress terms was presented by Boussinesq (1877) [15]. The author proposed that the contribution of turbulent stresses to momentum transfer be described in an analogous way to that observed by the action of the molecular

viscosity of the fluid, thus introducing the concept of turbulent viscosity, ν_t . Therefore, Boussinesq's hypothesis states that:

$$-\overline{u'_i(\mathbf{x}, t)u'_j(\mathbf{x}, t)} = \nu_t \frac{\partial \overline{u_i}}{\partial x_j} \quad (3.6)$$

There is clearly a direct analogy between the model proposed by Boussinesq and the molecular viscosity model, ν , for Newtonian fluids. However, in contrast to molecular viscosity, turbulent viscosity is not a property of the fluid, but of the flow, and therefore must include parameters that adequately characterize turbulent tensions in its formulation.

Over the last few years, Boussinesq's hypothesis, in a generalized form proposed by Kolmogorov (1942), has been widely used for modeling turbulent flows. According to Kolmogorov, the Reynolds tensor, in its general form, is expressed by:

$$-\overline{u'_i(\mathbf{x}, t)u'_j(\mathbf{x}, t)} = \nu_t \left(\frac{\partial \overline{u_i}}{\partial x_j} \frac{\partial \overline{u_j}}{\partial x_i} \right) - \frac{2}{3} \kappa \delta_{ij} \quad (3.7)$$

where δ_{ij} represents the Kronecker delta and the turbulent kinetic energy per unit mass.

Given this proposed framework, the last step for the definitive closure of the RANS equations is a turbulence model that will deal with the turbulent viscosity. In this work, the Spalart-Allmaras model will be used.

3.2 Spalart-Allmaras Model

The first turbulence model that showed widespread success and was used fairly widely in a variety of engineering disciplines was the $k - \epsilon$ model (1973) [17]. However, the model is not accurate at predicting boundary layer flows with adverse pressure gradients; which is particularly challenging for aerofoils and wings at high angles of attack, and for turbo-machinery applications. In addition, the $k - \epsilon$ model tends to get even worse when shocks are present because that increases the magnitude of the adverse pressure gradient.

In view of this, some notable models have been proposed in order to correct the deficiencies of $k - \epsilon$; among them are the $k - \omega$ model (1988) [18] and the Spalart-Allmaras model (1994) [3]. Due to the fact that it is described only by one equation - giving the opportunity for an in-depth study - this work will only deal exclusively with the latter.

3.2.1 Modified Eddy-Viscosity

The first notable feature of the Spalart-Allmaras model is the careful handling of the dynamics close to the wall. It is known that the value of y^+ varies linearly with the turbulent viscosity ν_t in the logarithmic region ($y^+ > 30$) (Fig. 3.1). However, in the sub-viscous layer ($y^+ < 5$), this profile is quartic, that is, $\nu_t \sim (y^+)^4$. This framework poses an inconvenience, as it requires substantially finer discretization for regions close to the wall.

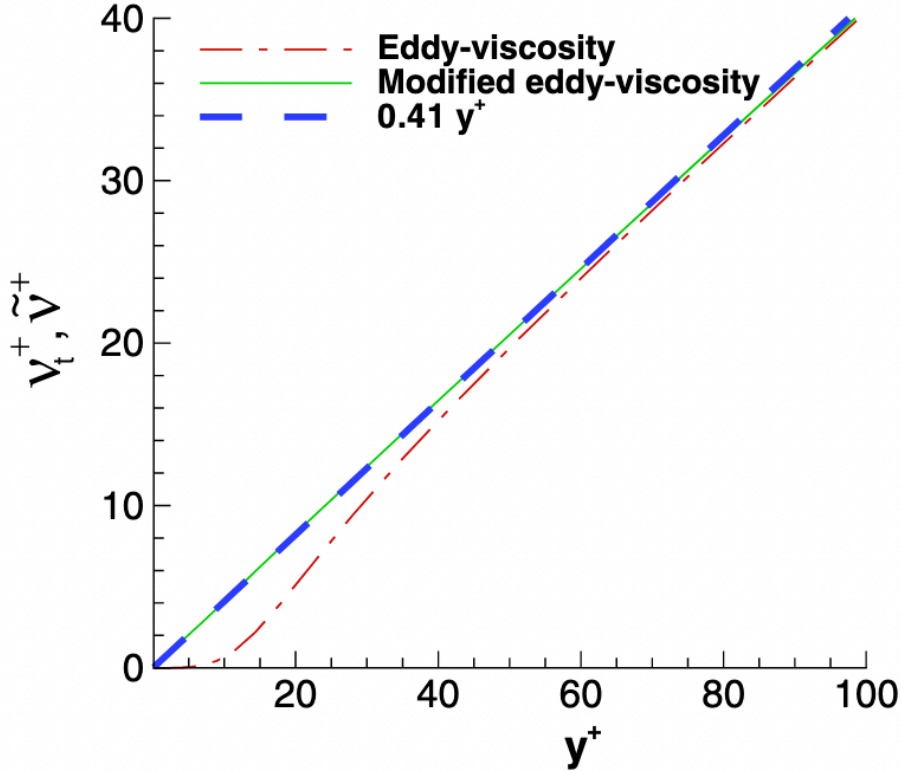


Figure 3.1: Eddy-viscosity v_t and modified eddy-viscosity \tilde{v} . [19]

Taking this into account, the Spalart-Allmaras model solves an equation not for v_t , but for \tilde{v} ; a modified eddy-viscosity. It remains perfectly linear both in the sub-viscous layer and in the logarithmic region, offering more numerical stability. This is done through the following transformation:

$$v_t = \tilde{v} f_{v1} \quad f_{v1} = \frac{\chi^3}{\chi^3 + c_{v1}^3} \quad \chi = \frac{\tilde{v}}{\nu} \quad (3.8)$$

where f_{v1} conveys a cubic behavior, alongside with viscous damping effects.

3.2.2 Turbulence Equation

We finally present the turbulence equation for the Spalart-Allmaras model:

$$\underbrace{\frac{\partial \tilde{v}}{\partial t} + \nabla \cdot (\mathbf{u} \tilde{v})}_{\text{Transport}} = \underbrace{c_{b1} \bar{S} \tilde{v}}_{\text{Production}} + \frac{1}{\sigma} \underbrace{[\nabla \cdot (\nu + \tilde{v}) \nabla \tilde{v} + c_{b2} (\nabla \tilde{v})^2]}_{\text{Diffusion}} - \underbrace{c_{w1} f_w \left(\frac{\tilde{v}}{d} \right)^2}_{\text{Destruction}} \quad (3.9)$$

- **Transport** - The first component of Eq.(3.9) is centered around the temporal derivative and the convection term. This component is fairly common in many transport equations and it allows us to convect the modified eddy-viscosity \tilde{v} across space and time.
- **Production** - The second term of the equation corresponds to the generation of turbulence in regions of high shear. The way that the model does this is by assuming that the generation is proportional to the effective shear rate \bar{S} in the mean velocity gradient.

- **Diffusion** - Regarding the diffusion term there are two main different components. The first one corresponds to the linear classic diffusion, as it can be seen in many other transport equations. However, there is an additional non-linear component that models more subtle phenomena. Particularly, this term was first introduced and calibrated to correctly account for the spreading of a wake profile, at the edge of the turbulent region [3]. Concerning other applications, this component will likely affect the behavior downstream of an airfoil or a diffusion section in a duct.
- **Destruction** - Finally, there is the destruction term. Physically, turbulence is mostly destroyed close to the wall through a combination of the inviscid blocking of pressure fluctuations from the unsteady turbulent field, and momentum damping due to viscosity. This explain the distance to the nearest wall d on the denominator, which will increase the effects of destruction as $d \rightarrow 0$. Additionally, the function $f_w \rightarrow 0$ as $d \rightarrow 0$, avoiding any mathematical inconsistencies.

However, the destruction term in Spalart-Allmaras only accounts for the inviscid blocking (pressure fluctuation damping). The viscous damping effect is built into the definition of $\tilde{\nu}$, as seen in Eqs.(3.8).

Now, one can say the closing problem is complete. In a short recap, the Spalart-Allmaras equation gives a robust estimate for the turbulent viscosity ν_t , which in turn closes the Reynolds stress tensor $-\overline{u'_i u'_j}$, completing the framework established by the modeling proposed by the RANS equations.

3.3 Transition Model

Despite the closure of the RANS equations using the Spalart-Allmaras model, many details intrinsic to the physics of the transition phenomenon are commonly neglected. Before employing data-driven methods - it is necessary to make use of every complementary tool available. For the phenomenon that underlies this work, the use of transition models is therefore justified.

In general, these models are coupled to classical turbulence models (ie. $k - \epsilon$) and act on the production term through a multiplicative factor. When in a laminar region, this factor will be null; inhibiting the effect of the turbulence model. On the other hand, it will allow the model to function fully when in a fully developed region. Additionally, it will allow a partial functioning of the turbulence model precisely in the region characterized by the transition.

One of the first models that served this purpose was the $\gamma - Re_\theta$ (2009) [20]; composed of two equations. Despite some theoretical problems, such as the lack of respect for Galilean invariance, this model inspired several others; as the BCM model [21], which will be used in this work. As mentioned above, this type of model relies on modification of the production term to provide transition to turbulence. Here, the production term is multiplied by the intermittency distribution function γ_{BC} :

$$\frac{\partial \tilde{\nu}}{\partial t} + \nabla \cdot (\mathbf{u} \tilde{\nu}) = \gamma_{BC} c_{b1} \overline{S} \tilde{\nu} + \frac{1}{\sigma} [\nabla \cdot (\nu + \tilde{\nu}) \nabla \tilde{\nu} + c_{b2} (\nabla \tilde{\nu})^2] - c_{w1} f_w \left(\frac{\tilde{\nu}}{d} \right)^2 \quad (3.10)$$

where the intermittency function is given as:

$$\gamma_{BC} = 1 - \exp(-\sqrt{T_1} - \sqrt{T_2}) \quad (3.11)$$

First, T_1 , is defined given as the following:

$$T_1 = \frac{\max(Re_\theta - Re_{\theta c}, 0)}{\chi_1 Re_{\theta c}} \quad (3.12)$$

where the value of the calibration constant χ_1 is 0.002 and the momentum thickness Reynolds number along with the vorticity Reynolds number and is given as:

$$Re_\theta = \frac{Re_{v,\max}}{2.193} \quad \text{where} \quad Re_v = \frac{\rho d_w^2 \Omega}{\mu} \quad (3.13)$$

And Re_{θ_c} is defined as the critical momentum thickness Reynolds number, which is a correlation that is based on the data gathered from several transition experiments, and indicates the emergence of transition.

In essence, this first term will check for the entire domain if $Re_\theta > Re_{\theta_c}$; and if so, T_1 will be activated. However, as it can be seen in Eq.(3.13), $Re_\theta = f(Re_v)$, and in turn, Re_v is a function of d , the wall distance. This means that for regions very close to the wall, T_1 will likely fail to indicate turbulent activity. That's why an additional term was added:

$$T_2 = \frac{\max(\chi_2 \frac{v_t}{v}, 0)}{\chi_2} \quad \text{where} \quad \chi_2 = 50 \quad (3.14)$$

Which will always return a significant value, specially for the boundary layer and regions near the wall. The values of the calibration constant χ_2 were found through numerical experimentation.

Finally, the modelling scheme is complete. In a quick recap, it is composed of the RANS equations, the Spalart-Allmaras turbulence model, and the BCM transition model. Given this, the next chapter will present some relevant details of the numerical implementation of this theoretical framework; in addition to preliminary results in an attempt to describe the aerodynamic forces caused by laminar separation flutter.

Chapter 4

Numerical Implementation

4.1 Introduction

After a complete understanding of the aspects related to classical problem modeling, this chapter will address some details regarding the numerical implementation. The mathematical formalism presented in this section serves not only for RANS simulations, within the framework presented in Chapter 3; but it was also used to generate the high-fidelity data discussed in Chapter 2.

First, the numerical domain will be displayed, including a discussion of boundary conditions. Next, the weak formulation of the equations presented so far will be discussed, and the importance of dealing with the problem in its variational form. With this, we will be able to present the Finite Element Method (FEM) and complementary details relevant to a consistent convergence of the results. Finally, preliminary results will demonstrate the shortcomings of the RANS-SA simulation (with the transition model), with respect to DNS high-fidelity data. This final discussion will be the main motivation for the adoption of data-driven techniques, using Data Assimilation in Chapter 5.

4.2 Methodology

4.2.1 Numerical Domain

We introduce the numerical boundary conditions used in the solution of the provided problems before presenting the weak formulation of the Navier-Stokes equations. An inlet frontier Γ_{in} will limit the unbounded physical domain upstream, while the other border Γ_{out} will limit the upper and lower zones at the outflow. The airfoil surface is still indicated by Γ_{lat} , and Figure 1.6 shows where these various borders are located. We will impose a null fluid velocity at Γ_{in} and a continuity velocity requirement at the fluid-structure interface since the airfoil is assumed to travel forward on a resting fluid. Along with a natural stress-free condition at Γ_{out} , is numerically closed as:

$$\mathbf{u}(\mathbf{x}, t) = 0 \quad \mathbf{x} \in \Gamma_{in} \quad (4.1)$$

$$\mathbf{u}(\mathbf{x}, t) = \mathbf{u}_w \quad \mathbf{x} \in \Gamma_w \quad (4.2)$$

$$\sigma(\mathbf{u}, p) \cdot \mathbf{n}_\infty = 0 \quad \mathbf{x} \in \Gamma_{out} \quad (4.3)$$

with \mathbf{n}_∞ the outward unit normal vector of the Γ_{out} borders.

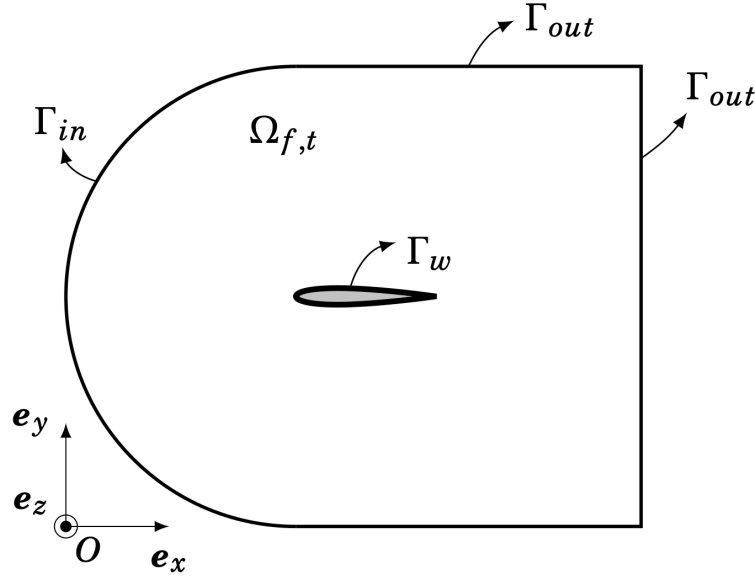


Figure 4.1: Schematic illustration of the computational domain for the simulation. Sabino et al. [2]

4.2.2 Weak Formulation

Originally the weak formulation has been introduced by mathematicians to investigate the behavior of the solution of partial differential equations, and to prove its existence and uniqueness. Later on, numerical schemes have been based on this formulation which lead to an approximate solution. The weak formulation is also called the variational formulation, where the solution satisfies a minimum of energy.

Taking the Navier-Stokes equations 2.2 as an example, we can define the state variables \mathbf{u} and p as belonging to the functional trial spaces $\mathcal{V}_{\mathbf{u}}^2$ and \mathcal{V}_p^1 , respectively:

$$\mathbf{u} \in \mathcal{V}_{\mathbf{u}}^2 \quad \text{with} \quad \mathcal{V}_{\mathbf{u}}^2 = \{\mathbf{a} \in \mathcal{H}^2(\Omega_f) | \mathbf{a}|_{\Gamma_{in}} = \mathbf{0}\} \quad (4.4)$$

$$p \in \mathcal{V}_p^1 \quad \text{with} \quad \mathcal{V}_p^1 = \{b \in \mathcal{H}^1(\Omega_f)\} \quad (4.5)$$

where \mathcal{H}^1 and \mathcal{H}^2 represent the Sobolev spaces. Concomitantly, we define the test functions \mathbf{v} and q in the test functional spaces $\mathcal{V}_{\mathbf{v}}^1$ and \mathcal{L}^2 as:

$$\mathbf{v} \in \mathcal{V}_{\mathbf{v}}^1 \quad \text{with} \quad \mathcal{V}_{\mathbf{v}}^1 = \{\mathbf{a} \in \mathcal{H}^1(\Omega_f) | \mathbf{a}|_{\Gamma_{in} \cup \Gamma_w} = \mathbf{0}\} \quad (4.6)$$

$$p \in \mathcal{L}^2 \quad (4.7)$$

where the test function \mathbf{v} is set to be zero on all Dirichlet conditions, where the solution is known. The weak formulation can be obtained by multiplying equations 2.2 by the test functions v and q , respectively, and integrate them over the domain Ω_f . One example that can be helpful to understand this procedure is the variational formulation of the Laplacian term:

$$\begin{aligned} -\Delta \mathbf{u} &= f & \text{in} & \quad \Omega \\ \mathbf{u} &= 0 & \text{on} & \quad \partial\Omega \end{aligned}$$

Introducing the test function \mathbf{v} , that belongs to $\mathcal{V}_{\mathbf{v}}^1$ (or \mathcal{H}_0^1 , this is, a regular Sobolev space that is null on the boundaries $\partial\Omega$), and integrating by parts:

$$-\int_{\Omega_f} \Delta \mathbf{u} \mathbf{v} = \int_{\Omega_f} \nabla \mathbf{u} \cdot \nabla \mathbf{v} = \int_{\Omega_f} f v + \int_{\partial\Omega_f} v \frac{\partial u}{\partial n} \text{ in } \Omega_f$$

where n is the unitary normal to Ω_f . And considering that $\mathbf{v} \in \mathcal{H}_0^1$, the problem becomes:

$$\int_{\Omega_f} \nabla \mathbf{u} \cdot \nabla \mathbf{v} = \int_{\Omega_f} f v$$

And so, applying this techniques and considerations to equation 2.2, we obtain:

$$\int_{\Omega_f} (\mathbf{u} \nabla) \mathbf{u} \mathbf{v} + \nu \nabla \mathbf{u} : \nabla \mathbf{v} - p \nabla \mathbf{v} - q \nabla \mathbf{u} = 0 \quad \forall \mathbf{v}, \forall q \quad (4.8)$$

Now, only derivatives of first order are involved in equation 4.8. The integration by parts operation lowers the order of the problem's maximum derivative and removes the prerequisite that $\mathbf{u} \in \mathcal{V}_{\mathbf{u}}^2$. Additionally, since the pressure variable doesn't require any derivatives, p no longer has to be a member of \mathcal{V}_p^1 .

Therefore, the problem can be restricted to the search of functions $\mathbf{u} \in \mathcal{V}_{\mathbf{u}}^1$ and $p \in \mathcal{L}^2$. The solution set has been expanded, hence the denomination weak form. If a solution of this weak form exists, then its uniqueness is proven by the Lax–Milgram theorem [22], key ingredient used to build the Finite Element Method.

Additionally, Newton's method is used to deal with the nonlinearities of the equation at the numerical level. This allows the problem to be posed as a linear problem, which is of high relevance for the use of the Lax-Milgram theorem.

4.2.3 Mesh Generation

Now for the space discretization we consider the partition of the fluid domain Ω_f into a finite number N_{ele} of closed disjoint D-dimensional elements \mathcal{K} , forming a discrete domain Ω_f^h , such that

$$\Omega_f^h = \bigcup_{e=1}^{N_{ele}} \mathcal{K}_e$$

The meshing method is based on a Delaunay triangulation method, carried out by the open-source software *FreeFem++* (REFFF Hecht, 2012), which is used to solve partial differential equations based on a discretization using the Finite Element Method, as explained in the next section.

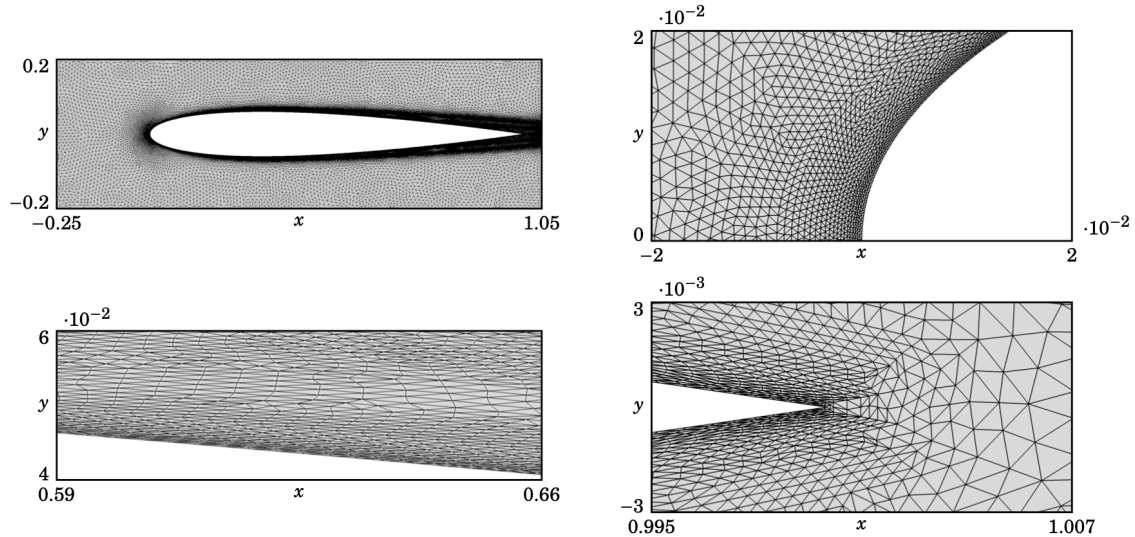
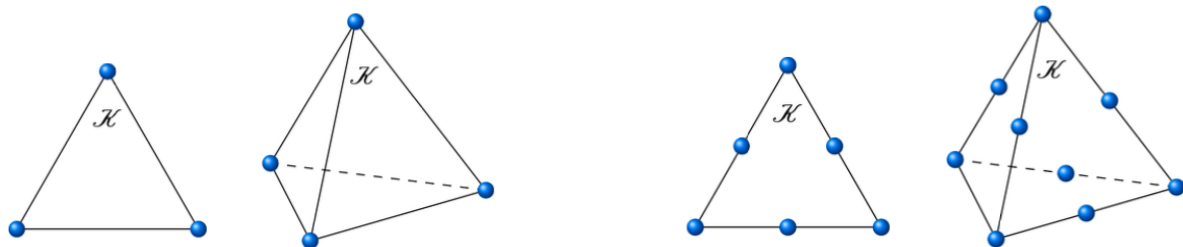


Figure 4.2: Two-dimensional triangular mesh around the NACA0012 airfoil, at $\alpha = 0^\circ$, on the top left, with the close-up views near the airfoil, on the bottom left, and near the leading and trailing edge zones, on the right. Sabino et al. [2]

The *FreeFem++* software restricts the elements \mathcal{K}_1 to simplex elements, such as triangles for two-dimensional meshes or tetrahedra for three-dimensional meshes. The software enables a local adaption based on a number of user-defined parameters, enabling an effective discretization method and the construction of an unstructured mesh.

Hecht et al. (1988) provides a description of the adaption algorithm. A metric matrix based on the Hessian of the user-defined fields determines the grid-point distribution of the resulting mesh. By setting the desired interpolation error of the fields on the new mesh, the precision of the adaptation (and consequently the grid-point density) can be managed. The minimum and maximum edge diameters as well as the anisometric coefficient are additional factors that can be specified.

The adopted mesh is unstructured and refined very close to the profile, where the huge gradients are likely to occur, and becomes increasingly coarse as it moves away from the profile. Moreover, it should be specified that throughout the study, once the profile becomes inclined (AOA > 0), it is the mesh that adapts and not the profile that moves.



(a) Degrees of freedom for a continuous piecewise linear finite element space P_1 . (b) Degrees of freedom for a continuous piecewise quadratic finite element space P_2 .

Figure 4.3: Two- and three-dimensional standard element cells: illustration of the number of degrees of freedom for the P_1 and P_2 finite element spaces. Sabino et al. [2]

4.2.4 Finite Element Method

Although structural engineers began using the finite element method (FEM) in the early 1940s (Courant, 1943), it was only in the late 1970s and early 1980s that it was made available to the fluid mechanics community (Babuka, 1973; Pironneau, 1989). With FEM, a solution to a differential equation is constructed from a series of local approximations. In that regard, we obtain approximations noted as $\mathbf{u} \approx \mathbf{u}^h$, $p \approx p^h$, $\mathbf{v} \approx \mathbf{v}^h$ and $q \approx q^h$.

We opted for the Taylor–Hood basis P_2^D/P_1 whose standard representation is present in figure 1.9. For a two-dimensional problem, one obtains, for each cell, 3 degrees of freedom for the pressure and 6 degrees of freedom per velocity component, whereas for a three-dimensional problem, one has 4 degrees of freedom for the pressure and 10 degrees of freedom per velocity component. Furthermore, we initially consider the Galerkin method (known as the Bubnov–Galerkin method) for the choice of the test functions. In this method, the test functions are chosen to be the same as the basis of the trial functions, such that:

$$\mathbf{v}^h(\mathbf{x}) = \sum_{j=1}^{N_{dof}^{\mathbf{u}}} \Phi_j(\mathbf{x}),$$

$$q^h(\mathbf{x}) = \sum_{j=1}^{N_{dof}^p} \Psi_j(\mathbf{x}),$$

Injecting the above decompositions into the discretised version of equation 4.8, one obtains the following discretised problem:

$$\begin{bmatrix} \mathbf{M}^{\mathbf{u}} & 0 \\ 0 & 0 \end{bmatrix} \frac{\partial}{\partial t} \begin{bmatrix} \mathbf{u}^h \\ p^h \end{bmatrix} + \mathbf{R}(\mathbf{u}^h, p^h) = 0 \quad (4.9)$$

with $\mathbf{M}_{ij}^{\mathbf{u}}$ being the mass matrix operator defined as:

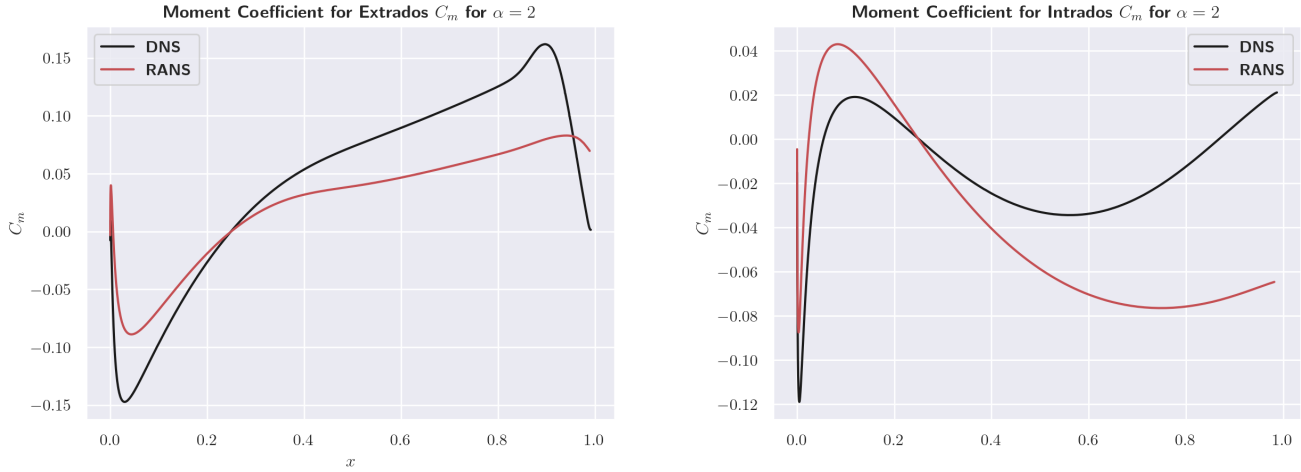
$$\mathbf{M}_{ij}^{\mathbf{u}} = \int_{\Omega_f^h} \Phi_i \Phi_j d\Omega_f^h \quad (4.10)$$

And \mathbf{R} being the residual operator, classically defined exactly as in [2].

4.3 Preliminary Results

Now, we can finally present comparative results between DNS (Chapter 2) and RANS-SA modeling (Chapter 3); that make use of the numerical methods presented in this chapter.

Analyzing exclusively the aerodynamic efforts, it is possible to perceive substantial differences between both results. Notably, for the momentum coefficient along the airfoil there is a worrying discrepancy at $\alpha = 2^\circ$. In Figure 4.4a, it is noted that the RANS-SA simulation fails to capture a considerable increment of this property around $x \approx 0.9$; which is precisely where the laminar separation bubble is located.



(a) Extradosal distribution of the moment coefficient C_m of RANS-SA. (b) Intradosal distribution of the moment coefficient C_m of RANS-SA.

Additionally, in Figure 4.4b, the disagreement between the results is not only quantitative, but qualitative as well. In the intradosal trailing edge, the momentum coefficient provided by DNS becomes positive again, while the RANS-SA simulation remains at negative values.

Since the Laminar Separation Flutter phenomenon is a self-sustained pitch oscillation, the moment coefficient is of great importance for an accurate description of the dynamics.

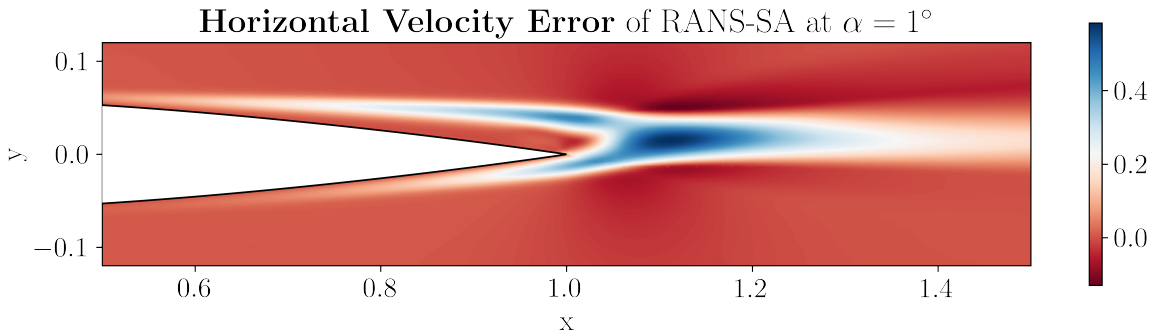


Figure 4.5: Direct subtraction of DNS and RANS-SA results for the horizontal velocity at $\alpha = 1^\circ$.

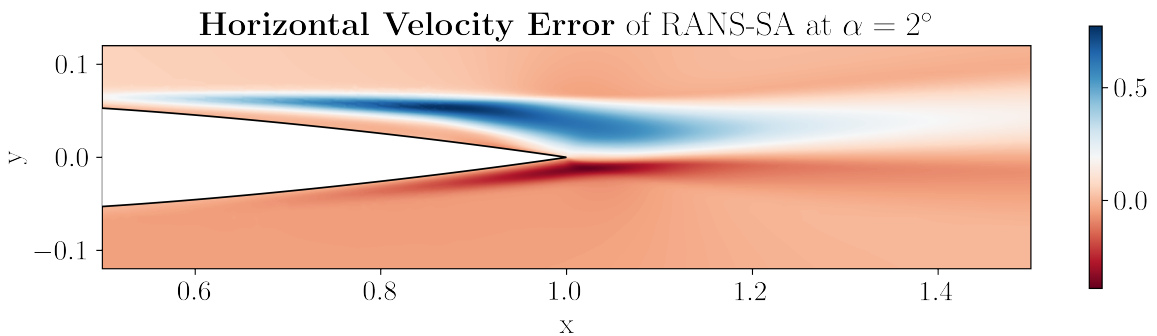


Figure 4.6: Direct subtraction of DNS and RANS-SA results for the horizontal velocity at $\alpha = 2^\circ$.

Another visualization that reinforces the disagreement of the results is the subtraction of the horizontal velocity field (DNS - RANS-SA). For angle $\alpha = 1^\circ$; there is a big difference in this property mainly in a region posterior to the trailing edge of the profile (Fig 4.5). For $\alpha = 2^\circ$, this discrepancy extends to the extradorsal part of the profile; immediately above the LSB (Fig 4.6).

Chapter 5

Data Assimilation

This chapter is devoted to formally presenting the data assimilation procedure and discussing the results obtained using a slightly modified framework from Chapter 3.

At first, a review will be made about the development of data assimilation methods; in order to understand the current paradigm. Next, different modeling approaches using Spalart-Allmaras as a foundation will be presented, along with a discussion of the different types of data that can be used to correct the original model. In sequence, the Field Inversion method will be presented in its complete mathematical formalism for the case previously discussed, in addition to details regarding the numerical implementation. Finally, the section dedicated to methodology ends with a discussion of complementary tools that provide critical notions about the modeling choices; such as sensitivity analysis and L-curves.

Consecutively, the results of this work will be presented. **The main objective of this chapter is to answer what is the optimal configuration for data assimilation modeling.** This includes choosing the control parameter, data type and optimal parameters for the cost function. Due to the extensive nature of the studies, two separate analyzes will be carried out, pointing out benefits and shortcomings of certain choices. Finally, a conclusive discussion will be made taking into account all the results obtained and different perspectives for data-driven models.

5.1 Introduction

There is nothing new in the idea of using high-fidelity data to correct models. As we know, no model provides a perfect description of reality; having its limits in the description of a finite amount of effects and in a specific regime of physical parameters. In many instances, the model correctly proposes that the dynamics of a phenomenon obeys a specific mathematical framework. Nonetheless, it leaves some open constants or functions that will be calibrated by means of experimental data, and that will allow an optimal fit of the model to the phenomenon. This can be easily seen in Spalart-Allmaras (Eqn. 3.9) in constants such as c_{b1} , c_{b2} and c_{w1} .

However, this is not data assimilation. This technique, developed primarily in the fields of meteorology and oceanography [23] [24], reinforces a much more intricate relationship between data and a base model. The combination of these two components can be used to obtain a better description of the model inputs like initial condition, boundary conditions or a control parameter [25] [26]; in addition to also demonstrating high efficacy to complete sparse experimental observations [27].

The first use of data-assimilation can be traced back to Kalman et al. [28], where an estimation of the whole state of the system from limited partial measurements was needed in order to act on the system with a control law, stabilizing it. The Kalman filter is the design of such observer so that its prediction is as close as possible to the current state. The final form of this filter can be seen as

a prediction step, where the model of the dynamical system is applied on the a priori state, and a correction step, where the external data (or measure) is taken into account through the filter, which is constructed based on the covariance matrix of the state vector.

This technique has been applied for several purposes in fluid mechanics, such as the estimation of velocity field from Particle-Tracking Velocimetry snapshots in a planar-jet configuration at $Re = 2000$ [29], the recovery of low-Reynolds wall-bounded turbulent flows from wall measure [30], estimation of Mach number, angle of attack and eddy-viscosity field at high Reynolds number flows in complex flow configuration [26].

Another class of DA is tied to variational methods (VDA) [31], which are based on the use of the optimal control theory [32] to minimize the error between observations of a reference flow and a numerical estimation. One of the earliest applications of this technique was on the weather forecast problem (Talagrand and Courtier, 1987 [33]) under the name of 3D/4D-Var where the tuning parameters were the initial condition of the dynamical model such that some cost, function of the error between the model's prediction and the external data, is minimal.

Concerning the VDA approach, the numerical simulations of turbulent flows over complex geometries are mostly achieved with the Reynolds-averaged Navier-Stokes (RANS) equations and turbulence models - as presented in Chapter 3 - thus promoting the low computational cost over the accuracy. Among these, one can distinguish gradient-based optimization (Foures et al. [34], Symon et al. [35]) and ensemble-based optimization (Iglesias et al. [36], Kato and Obayashi [26]). More particularly, Foures et al. [34] studied a low-Reynolds cylinder flow [$Re = \mathcal{O}(10^2)$] exhibiting vortex shedding. They tuned a volume force acting in the steady Navier-Stokes equations such that its corresponding solution best matches velocity measurements, mimicking a real experimental situation where such measurements are provided by a PIV setup.

At even higher Reynolds numbers, the RANS equations supplemented with a turbulence model is a reasonable choice for the baseline model, as discussed in Chapter 3, since they usually provide solutions that aim at approximating the turbulent mean flow. For instance, Li et al. [37] optimized a set of coefficients in a $k - \omega$ RANS model to match as closely as possible the given high-fidelity data.

Furthermore, Duraisamy et al. [4] employed gradient-based optimization techniques to tune spatially dependent production terms in turbulence models, so as to recover mean-flow data obtained by DNS or experiments. This specific procedure is also known as the Field Inversion method; and it has been widely used as an intermediate step of machine learning-corrected RANS models, which will be presented in Chapter 5. In more recent works, Franceschini et al. [5] showed that the data-assimilation procedure allowed an almost exact recovery of the mean-flow over a backward-facing step. Contrary to a scalar correction source term in the equations governing the turbulent scales, the vectorial momentum correction term allows for a much more flexible model to accommodate the prescribed mean-flow feature.

In all referenced works, there are non-trivial choices regarding the level of freedom given to correction. Those can provide excellent results, however at the cost of completely evading the physics proposed by the base model. This work values a careful analysis of these choices and presents a comparative study of several possibilities within the Field Inversion framework. Given this, results of a modeling similar to Duraisamy [4] will be discussed with the control parameter in all possible terms of the turbulence equation (Eqn. 3.9); and not just in the term of production. The correction with the term source will also be presented, inspired by the work of Franceschini [5].

5.2 Methodology

In this section a presentation will be carried out regarding the corrections to the base model proposed by this work. Next, the mathematical formalism of variational data assimilation will be

introduced; in addition to the low-memory BFGS algorithm [38] for the numerical computation of the cost-functional minimum.

Subsequently, techniques with the potential to provide complementary analyzes to the proposed correction will be presented. Not only do they allow a robust choice of optimal parameters linked to optimization, but they also allow a critical comparative understanding of the different corrections.

5.2.1 Modified Spalart-Allmaras Modelling

Now, we make a quick review of the equations that compose the modeling framework proposed in this work, taken from Chapters 2 and 3. We use a simplified Navier-Stokes model in which the chaotic and complex character of turbulence is seen as a superposition of a behavior mean and statistical fluctuations, modeling RANS (Eqn. 3.5). The fluctuations that could not be closed by this modeling are framed within the Boussinesq hypothesis (Eqn. 3.7), which introduces a new variable: turbulent viscosity. In turn, we use the Spalart-Allmaras turbulence model to solve this variable (Eqn. 3.9), thus closing the problem. Finally, given the particularities of the physical phenomenon studied, we use a transition model (Eqn. 3.10). This enables the production of turbulence the possibility of being fully functioning, partially active or null, depending on the spatial region. We can quickly present once again these three equations as:

$$\bar{\mathbf{u}} \cdot \nabla \bar{\mathbf{u}} + \nabla \bar{p} = \nabla \cdot [(\nu + \nu_t(\tilde{\nu})) \nabla \bar{\mathbf{u}}] \nabla \cdot \bar{\mathbf{u}} = 0 \quad (5.1)$$

$$\bar{\mathbf{u}} \cdot \nabla \tilde{\nu} = s(\tilde{\nu}, \nabla \tilde{\nu}, \nabla \bar{\mathbf{u}}) \quad (5.2)$$

Where the production, diffusion and destruction term of the Spalart-Allmaras model are condensed in the term $s(\tilde{\nu}, \nabla \tilde{\nu}, \nabla \bar{\mathbf{u}})$.

The first correction to the Spalart-Allmaras model that we present does not propose the addition of any term. This correction, by contrast, focuses on the boosting or diminishing of the different terms of the original equation; thus providing a physical understanding of the modification. For this technique, we explicitly show the four terms inside $s(\tilde{\nu}, \nabla \tilde{\nu}, \nabla \bar{\mathbf{u}})$:

$$\underbrace{\bar{\mathbf{u}} \cdot \nabla \tilde{\nu}}_{\text{Transport}} = \underbrace{\beta_{prod} \gamma_{BC} P(\tilde{\nu})}_{\text{Production}} + \underbrace{D_1 (\beta_{diff}, \tilde{\nu}, \nabla \tilde{\nu})}_{\text{Diffusion}} + \underbrace{\beta_{cross-diff} D_2(\tilde{\nu})}_{\text{Cross-Diffusion}} - \underbrace{\beta_{des} E(\tilde{\nu})}_{\text{Destruction}} \quad (5.3)$$

In the equation 5.3. the terms P , D_1 , D_2 and E refer to the terms of production, linear diffusion, cross-diffusion and destruction; presented in the equation 3.9. In this new equation, we present the 4 corrective control parameters concomitantly: β_{prod} , β_{diff} , $\beta_{cross-diff}$ and β_{des} . However, for each test performed, only one parameter will be chosen to be corrected, while the others will be 1 in the entire space. Furthermore, we reiterate the choice of splitting the diffusion term in two; which is supported by the discussions made in Chapter 3.

At this point, several questions can already be asked. Among them, it is natural to ask which corrective parameter presents better results. And what physical sense can these results bring? And even with these answers, it is possible to ask how valid it is to extrapolate these analyzes to physical scenarios other than the laminar separation flutter.

Another corrective modeling that can be proposed now adds additional terms to the turbulence equation, acting as forces:

$$\bar{\mathbf{u}} \cdot \nabla \tilde{\nu} = s(\tilde{\nu}, \nabla \tilde{\nu}, \nabla \bar{\mathbf{u}}) + \tilde{f}_{\tilde{\nu}} \quad (5.4)$$

This approach was proposed by Franceschini et al. [5], and implies a modification in the balance between the terms in Spalart-Allmaras; changing the eddy viscosity ν_t . And therefore having only

an indirect effect on the velocity $\bar{\mathbf{u}}$ and the pressure field \bar{p} . Unlike other techniques present in the literature, this method preserves the Boussinesq assumption, which is in agreement with the analyzes made in Chapter 1.

Because it is not restricted to any previously defined term, this additional force proves to be substantially more flexible to make significant corrections and changes in flow. As will be seen in the following subsections, despite the accuracy of the correction, this approach is more likely to present results that devoid of physical argumentation. This issue will be one of the major discussions of this work, and a robust comparative study will be carried out in order to denote the advantages and shortcomings of each technique.

Finally, a subtle variation is proposed in this work for equation 5.4, which consists of multiplying the additional forcing term by the modified turbulent viscosity:

$$\bar{\mathbf{u}} \cdot \nabla \tilde{v} = s(\tilde{v}, \nabla \tilde{v}, \nabla \bar{\mathbf{u}}) + \tilde{f}_{\tilde{v}} \tilde{v} \quad (5.5)$$

This subtle correction brings significant changes, and will be duly supported and grounded in subsection 5.4.3.

5.2.2 Variational Data Assimilation

Now, once the general idea of how the correction will act in the base model has been presented, it is necessary to understand how the correction is obtained for each point in space. Let m be a set of higher-fidelity or experimental measurements that correspond to information extracted from the flow and $\mathcal{M}(\cdot)$ the measurement operator that allows to extract the corresponding measure from the DNS simulation. For a high-fidelity data \mathbf{q} of any nature, this operator would be \mathbf{q} , yielding $\mathcal{M}(\mathbf{q}) \in M$, where M is the measurement space, whose norm is given, generically, by $\|\cdot\|_M$. The data-assimilation problem can now be recast into an optimization one, in which the control parameter β (either a multiplicative coefficient or an additional forcing) will be tuned such that the cost functional

$$\mathcal{J}(\mathbf{q}) = \frac{1}{2} \|\mathcal{M}(\mathbf{q}) - \bar{\mathbf{m}}\|_M^2 + \frac{\alpha_{pen}}{2} \|\beta - 1\|_M^2 \quad (5.6)$$

is minimal, having as constraints the RANS-SA Eqs. 3.5 and 3.9. In equation 5.6 we also remark the addition of a penalty term for the correction, weighted by α_{pen} . This is important, as we are not only looking for a control parameter that provides a solution that is closer to the reference data, but that does so in the least intrusive way possible.

Following [38], this optimization problem may be solved with an iterative gradient-based algorithm. It requires in particular the computation of the cost functional gradient with respect to the correction fields, $\nabla_{\beta} \mathcal{J}$. To obtain an expression of the gradient, we resort to a Lagrangian formalism, that allows rewriting the constrained optimization problem into an unconstrained optimization problem. To that aim, the state is augmented with a set of Lagrange multipliers (or adjoint variables) $(\bar{\mathbf{u}}^{\dagger}, \bar{p}^{\dagger}, \tilde{v}^{\dagger})$ and we look for critical points of the Lagrangian functional:

$$\begin{aligned} \mathcal{L}([\bar{\mathbf{u}}, \bar{p}, \tilde{v}], [\bar{\mathbf{u}}^{\dagger}, \bar{p}^{\dagger}, \tilde{v}^{\dagger}], \beta) &= \mathcal{J}(\bar{\mathbf{u}}) \\ &\quad - (\bar{\mathbf{u}}^{\dagger}, \bar{\mathbf{u}} \cdot \nabla \bar{\mathbf{u}} + \nabla \bar{p} - \nabla \cdot ((\nu + \nu_t(\tilde{v})) \nabla \bar{\mathbf{u}}))_{\Omega} \\ &\quad - (\bar{p}^{\dagger}, \nabla \cdot \bar{\mathbf{u}})_{\Omega} \\ &\quad - (\tilde{v}^{\dagger}, \bar{\mathbf{u}} \cdot \nabla \tilde{v} - s(\tilde{v}, \nabla \tilde{v}, \nabla \bar{\mathbf{u}}) - \beta)_{\Omega} \end{aligned} \quad (5.7)$$

where $(q_1, q_2)_\Omega = \int_\Omega q_1 \cdot q_2 d\Omega$ represents the inner product related to the classical L_2 norm. And considering the Lagrangian formalism, setting to zero the variation of the Lagrangian with respect to the adjoint variables $[\bar{\mathbf{u}}^\dagger, \bar{p}^\dagger, \tilde{v}^\dagger]$ will yield the governing equations 5.1 and 5.2. On the other hand, setting to zero its variation with respect to the direct variables $[\bar{\mathbf{u}}, \bar{p}, \tilde{v}]$ provides de adjoint equations of the RANS-SA model. We remark that, although we present the continuous formalism, in practice, we solve the discrete adjoint matrix, consisting in the transpose of the Jacobian matrix.

Taking now the variation of the Lagrangian with respect to the control parameter terms, and considering firstly the multiplicative correction, we have:

$$\left(\frac{\partial \mathcal{L}}{\partial \beta}, \delta \beta \right)_\Omega = -(\tilde{v}^\dagger, \delta \beta)_\Omega \longrightarrow \nabla_\beta \mathcal{J} = -\tilde{v}^\dagger T_{SA} \quad (5.8)$$

In which T_{SA} corresponds to the Spalart-Allmaras' term that was chosen to be corrected. Considering now the additional forcing approach, one would find:

$$\left(\frac{\partial \mathcal{L}}{\partial \mathbf{f}}, \delta \mathbf{f} \right)_\Omega = -(\tilde{v}^\dagger, \delta \mathbf{f})_\Omega \longrightarrow \nabla_{\mathbf{f}} \mathcal{J} = -\tilde{v}^\dagger \quad (5.9)$$

Therefore, when using the additional force only the adjoint of the modified eddy-viscosity will determine the region that will most probably be affected after the correction. With this gradient information we are able to proceed with the implementation of the BFGS method.

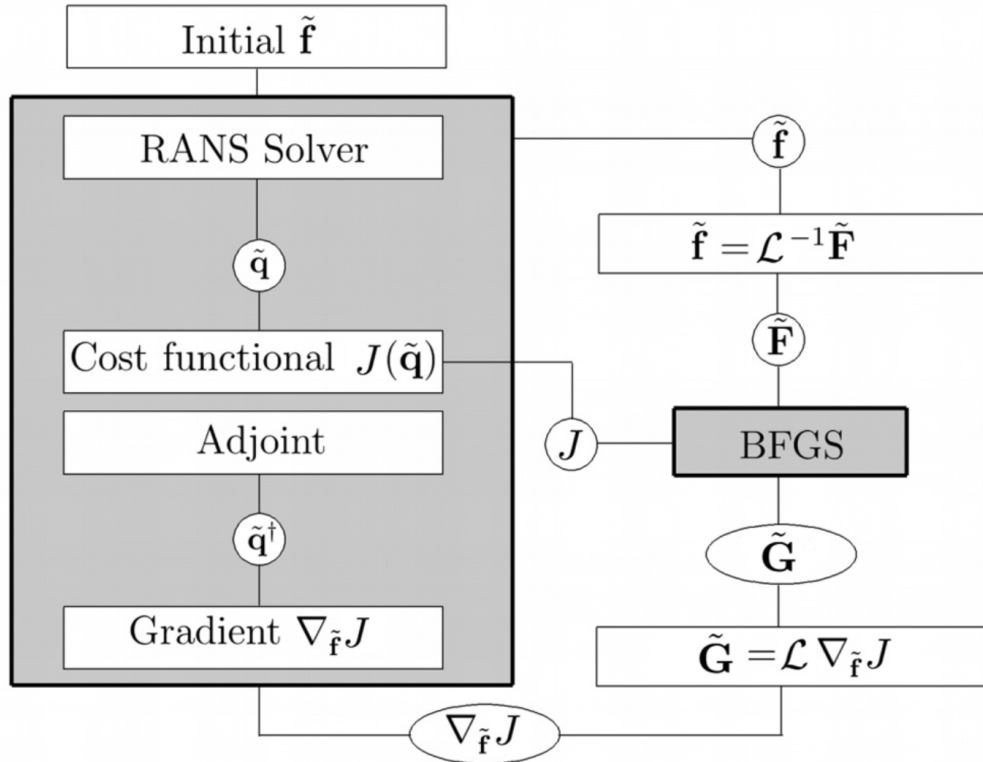


Figure 5.1: Sketch of the BFGS algorithm for a general problem, having \mathbf{f} as a control parameter and \mathbf{q} as state. The adjoint variable is denoted by \mathbf{q}^\dagger . Franceschini et al. [5]

The low-memory BFGS provides a second-order convergence, outperforming, in general, simple gradient descent methods. This higher-order convergence is achieved through an approximation of

the Hessian $\mathcal{H} = \nabla_F \nabla_F \mathcal{J}$, which contains the second-order derivatives of the cost functional \mathcal{J} with respect to a generic forcing vector F , for the case of a correction that uses an additional forcing. This approximation is then used to find the descent direction by solving $\mathcal{H}_n^{-1} \tilde{\mathbf{G}}_n$, where $\tilde{\mathbf{G}}_n$ is the numerical gradient at iteration n . This matrix is approximated through:

$$\mathcal{H}_{n+1} = \mathcal{H}_n + \frac{\mathbf{y}_n \mathbf{y}_n^T}{\mathbf{y}_n^T \mathbf{s}_n} - \frac{\mathcal{H}_n \mathbf{s}_n \mathbf{s}_n^T \mathcal{H}_n}{\mathbf{s}_n^T \mathcal{H}_n \mathbf{s}_n} \quad (5.10)$$

with $\mathcal{H}_0 = \mathcal{J}$, $\mathbf{y}_n = \tilde{\mathbf{G}}_{n+1} - \tilde{\mathbf{G}}_n$ the difference of the gradient between two successive iterations and $\mathbf{s}_n = \mathbf{F}_{n+1} - \mathbf{F}_n$ the difference in forcing vectors. A sketch of the coupling of the BFGS method with our finite-element flow solver is shown in Fig. 5.1.

It is worth-mentioning that the optimization algorithm remains in the vicinity of the initial (baseline laminar) condition when the BFGS method is used without correcting the gradient direction (setting $\mathcal{L} = \mathcal{J}$ in Fig. 4). This shows that informing BFGS algorithm the metric of the mesh is crucial for the proper convergence of BFGS.

5.2.3 Tools and Techniques

As mentioned earlier, we will now discuss complementary techniques and analyzes that will inform important choices about modeling. These choices imply choosing the control parameter, the type of data to be used and even parameters intrinsic to the optimization, such as the α_{pen} penalty.

Sensitivity Analysis

A substantially powerful technique for optimization problems is sensitivity analysis. It essentially consists of the results obtained in the equations 5.8 and 5.9, when computing the Lagrangian with respect to the control parameter.

More particularly, by obtaining the gradient of the cost function with respect to the control parameter, we gain an understanding of the regions that, when affected by the control parameter, will allow a greater variation of the functional cost. This reflects, therefore, the areas that are most likely to be affected by the control parameter after assimilation.

Among the different advances obtained by this technique, we highlight the study that was made when varying the type of data used for assimilation. Objectively, there is no reason to expect the correction to be the same when using the pressure coefficient distribution rather than the skin drag coefficient; or the velocity field. However, the proposed idea is actually verified; there is an invariance in the area of correction in relation to the use of parietal data C_p , C_m , C_f and velocity field data \mathbf{u} .

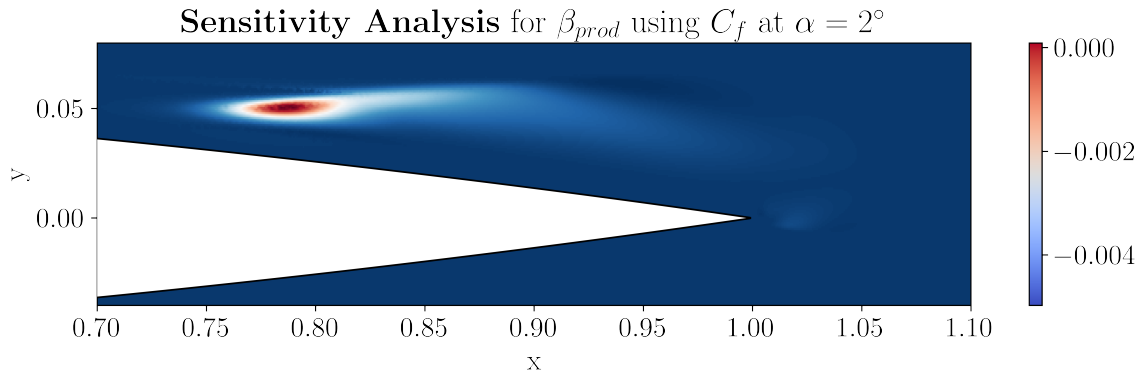


Figure 5.2: Sensibility analysis using parietal data C_f at $\alpha = 2^\circ$.

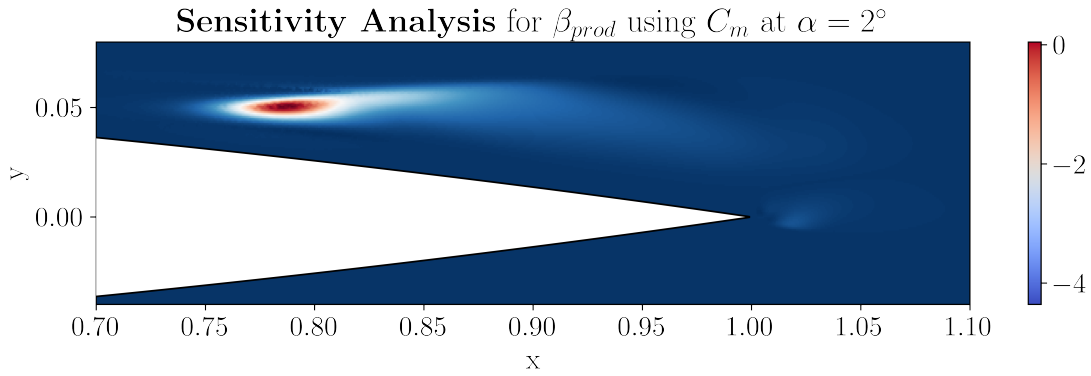


Figure 5.3: Sensibility analysis using parietal data C_m at $\alpha = 2^\circ$.

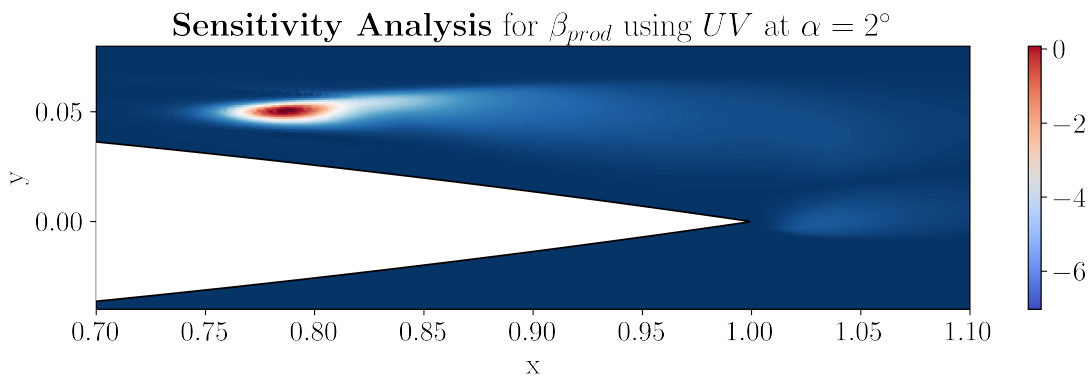


Figure 5.4: Sensibility analysis using full field data UV at $\alpha = 2^\circ$.

This result can be readily seen in Figs 5.2, 5.3 and 5.4; in which the sensitivity analysis is performed for the correction in the production term at an incidence of 1° . We reinforce, however, that although the area of activity remains the same, the assimilation capacity can vary drastically depending on the data used. This is due to differences in the intensity of the correction produced in order to focus on certain data; and the ability of the data to provide details intrinsic to the phenomenological complexity of the problem.

In the next subsection, this technique will be taken up again in order to complement different results; explaining eventual failures and possible successes of the correction parameter choice.

L-Curves

A last technique that is of great help in this work is the L-Curves analysis. The L-curve is a log-log plot of the norm of a regularized solution versus the norm of the corresponding residual norm. It is a convenient graphical tool for displaying the trade-off between the size of a regularized solution and its fit to the given data, as the penalization parameter α_{pen} varies. The L-curve thus gives insight into the regularizing properties of the underlying regularization method, and it is an aid in choosing an appropriate penalization parameter for the given data.

That is, in practical terms, the L-curves compare the magnitude of the residual between high-fidelity data and simulation data and the magnitude of the correction parameter. This allows choosing a penalty parameter α_{pen} that works as a compromise between both quantities. On the one hand, we want to reduce the residue as much as possible; nevertheless, we prioritize that this reduction be mediated by a correction that is as intrusive as possible.

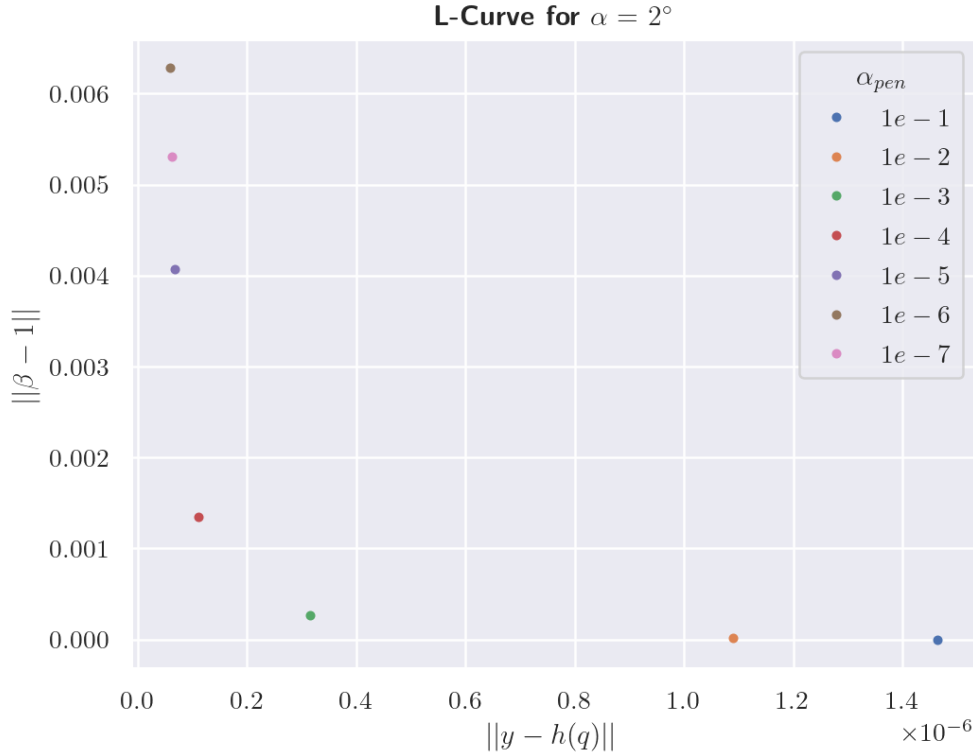


Figure 5.5: L-curve analysis for assimilations performed using C_f parietal data for the correction of the production term β_{prod} ; at $\alpha = 2^\circ$.

As an example, we see that a penalty $\alpha_{pen} = 10^{-5}$ presents itself as the ideal compromise between these two scales when we specifically study the control parameter acting on the production term, using the skin friction coefficient at an incidence of $\alpha = 2^\circ$.

5.3 Results: Scenario I

5.3.1 Motivation

As discussed, due to the extensive comparative scope of this work, the results will be divided into two scenarios. In this first step, the objective is to present the results obtained using only parietal data (C_p , C_f and C_m), and being applied exclusively to the optimization of multiplicative control parameters in the turbulence equation. It can be considered that this scenario proposes a more "strict" modeling in the face of scarcity of data.

From a practical point of view, this limited approach is of high value for two reasons. The first is linked to the replicability of this method, since there is a vastly greater amount of parietal data available - either experimentally or numerically - than measurements of the complete velocity field. By proving that accurate corrections can be obtained within this scope of data scarcity, one denotes the strength and potential of this method for many other applications.

The other relevant concern is related to the degree of freedom given to the correction parameter. In many studies, excellent results were obtained through control parameters that act as additional forcings in the turbulence equation (Eqn. 3.9), or even in the momentum equation (Eqn. 2.2). Despite the accuracy, these models often offer corrections without physical insight, just fitting the data provided. With the single restriction on multiplicative control parameters (β_{prod} , β_{diff} , $\beta_{cross-diff}$

and β_{des}) in the original terms of Eqn. 3.9, one grants more interpretability to the assimilated result, in addition to ensuring that the founding hypotheses of the base model are respected.

Finally, this analysis proposes to compare 4 control parameters, using 3 different data sources for 5 angles of attack. Given these 60 results obtained, for organizational reasons, the comparative study begins by setting the angle of attack at $\alpha = 2^\circ$; which has the greatest discrepancy between the RANS and DNS results, as discussed in Chapter 4.

5.3.2 Analysis for $\alpha = 2^\circ$

As mentioned earlier, this first step of the analysis aims at a complete comparison of all control parameters and all types of parietal data; setting only the angle of attack to $\alpha = 2^\circ$. Among the metrics used to evaluate the assimilated results, there is notably the reduction of the cost function (Eqn. 5.6); in addition to the L_2 error :

$$L_2 \text{ error} = \int_{\Omega} (u_{DNS} - u_{DA})^2 + (v_{DNS} - v_{DA})^2 d\Omega$$

However, the values for the L_2 error (in red) are normalised with respect to the L_2 error of the original RANS-SA simulation, used as the first guess for the optimization process. Given this, we present below the value of the post-assimilation cost function and the error under the L_2 norm:

Observation	Control Parameter			
	β_{prod}	β_{diff}	$\beta_{cross-diff}$	β_{des}
Moment Coefficient	4.03e-3	2.62e-3	3.19e-3	4.83e-1
	7.38e-2	6.58e-2	7.49e-2	3.51e-1
Pressure Coefficient	1.95e-3	1.71e-2	3.41e-3	1.59e-1
	7.32e-2	9.08e-2	7.60e-2	1.69e-1
Skin Friction Coefficient	3.87e-2	6.53e-2	7.43e-2	2.45e-1
	6.69e-2	1.00e-1	8.23e-2	2.31e-1
Average Reduction	1.88e-2	2.83e-2	2.72e-2	2.95e-1

Table 5.1: Final values for the cost function (black) and the velocity error of the field under the L_2 norm (red) for every observation and control parameter at $\alpha = 2^\circ$, using $\alpha_{pen} = 10^{-7}$.

In view of these results, several conclusions can be drawn:

- Clearly, the control parameter value acting on the destruction term β_{des} is substantially less effective in its corrections than any other parameter. This result is shown consistently and regardless of the type of data used. In a more representative view, this fact can be clearly seen in the correction of the extradorsal distribution of the moment coefficient, using the pressure coefficient as an observation.

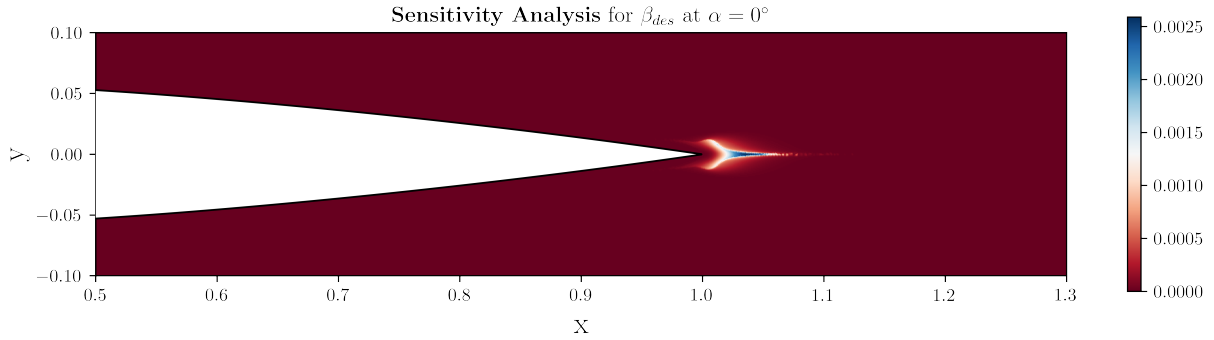


Figure 5.6: Sensitivity Analysis with respect to the control parameter acting on the destruction term.

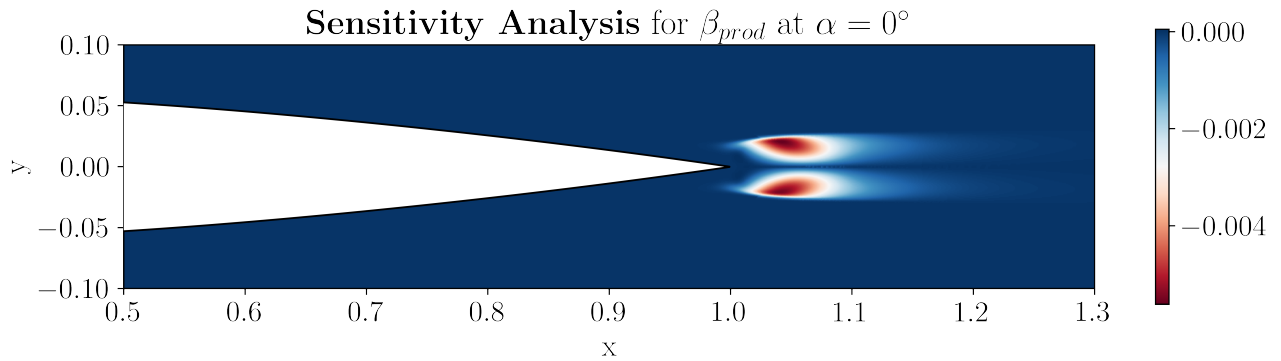


Figure 5.7: Sensitivity Analysis with respect to the control parameter acting on the production term.

And indeed, in the face of a sensitivity analysis of the gradient of the cost function in relation to the destruction term, an extremely limited spatial influence is perceived (Fig. 5.6). When comparing with the same analysis for the terms of production (Fig. 5.7); one may notice that the destruction term fails to change significant behaviors near the laminar separation bubble. Therefore, this term will be discarded as an option for assimilations.

- Considering now the other control parameters, the similarity between the results provided by the correction in diffusion and in cross-diffusion is remarkable; with a slight advantage for cross-diffusion. This can also be clearly seen in Figure 5.8. In addition, the cross-diffusion term has a non-linear character, unlike production and the classical diffusion term. In view of this particularity, and in order to narrow the analysis, the classic diffusion term will be absent in subsequent analyses.
- Finally, it is necessary to discuss the differences between the different types of data used. It is remarkable the consistency of the results when using the moment coefficient as an observation for the assimilation. However, for the scope that is relevant to this work, it can be said that the pressure coefficient presents results as good as it. This makes sense, since from a physical point of view, they tend to capture the same dynamics. And considering the availability and greater experimental ease of obtaining data for the pressure coefficient, we will proceed with it at the expense of the moment coefficient.

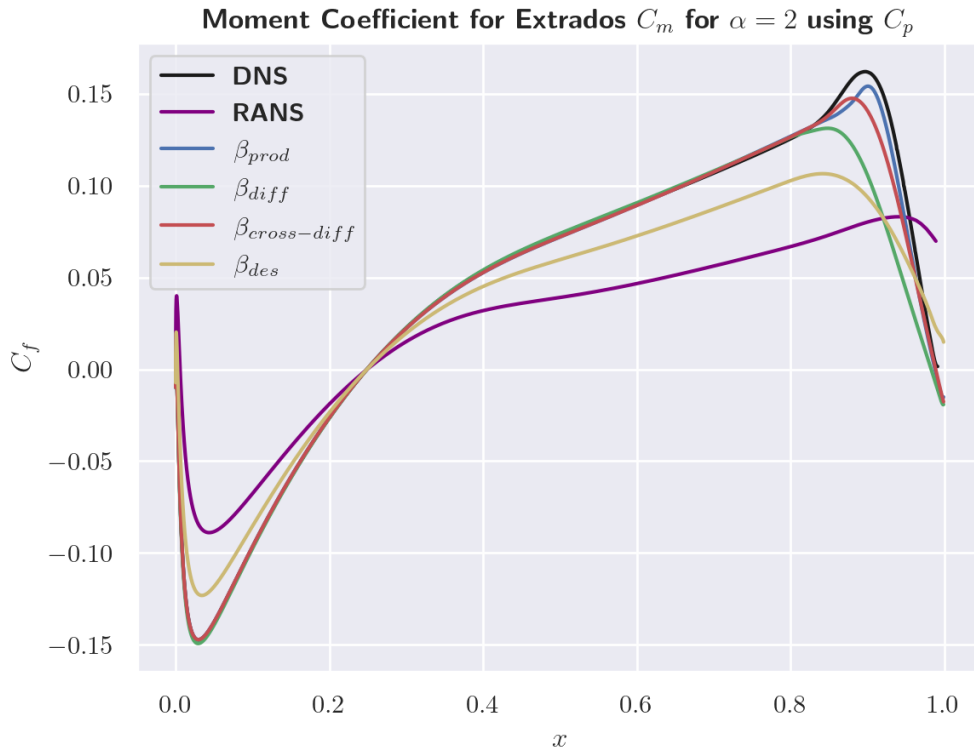
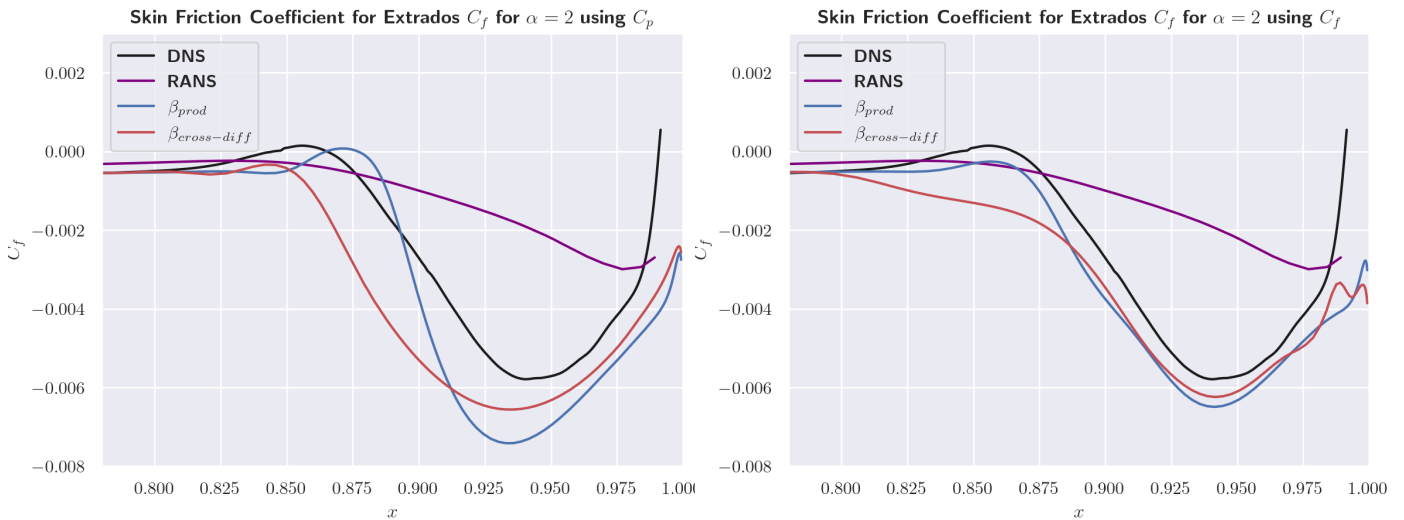


Figure 5.8: Complete comparison of control parameters for the description of the extradorsal moment coefficient using C_p at $\alpha = 2^\circ$

Regarding the skin friction coefficient, it is clear that it does not present results as consistent as the other two candidates. However, it is the only data that robustly fits the extradorsal skin friction distribution (as it should). This can be seen in the comparison of Figures 5.9a and 5.9b; in which C_p and C_f were used, respectively.



(a) Extradorsal skin friction coefficient at α° described by an assimilation using C_p . (b) Extradorsal skin friction coefficient at α° described by an assimilation using C_f .

Taking these results into consideration, it is difficult to clearly point out which is the optimal configuration in terms of the control parameter and type of observation used for assimilation. We remain with the pressure and skin friction coefficients; and with the corrective terms in production and cross-diffusion.

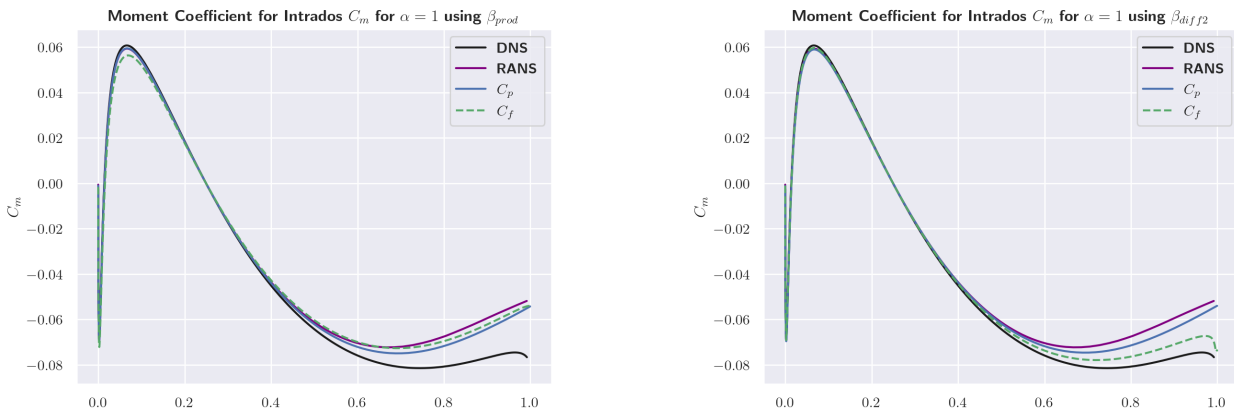
In order to gain more insights into the robustness and consistency of these possible combinations, it is necessary to analyze other aerodynamic regimes. Despite the richness of detail and the difference between RANS and DNS results for $\alpha = 2^\circ$, there is possibly greater dynamic complexity occurring at $\alpha = 1^\circ$. This is due to the fact that this angle is the threshold for the emergence of the LSB, in addition to marking the beginning of a completely different stability regime [2].

5.3.3 Analysis for $\alpha = 1$

We now proceed with an analysis of the same nature as in the previous subsection, but for $\alpha = 1^\circ$. For the reasons mentioned, we restricted the data used only to the coefficient of skin friction and pressure; and we deal with them exclusively for the optimization of the control parameters acting on the production and cross diffusion term. With this, we obtain the table 5.2, in which we only compare the reduction of the cost function.

Observation	Control Parameter	
	β_{prod}	$\beta_{cross-diff}$
Pressure Coefficient	5.27e-1	6.05e-1
Skin Friction Coefficient	3.09e-1	5.15e-2

Table 5.2: Final values for the cost function at $\alpha = 1^\circ$.



(a) Extradorsal moment coefficient at $\alpha = 1^\circ$ using β_{prod} . (b) Extradorsal moment coefficient at $\alpha = 1^\circ$ using $\beta_{cross-diff}$.

Here, we have a surprising result exclusively for the assimilation that uses the skin friction data versed for the optimization of the parameter acting in the cross-diffusion term. This result is reinforced in bold in the table. Complementarily, one can more substantially perceive this difference in the curves for the moment coefficient (Figure 5.10a and 5.10b).

It is truly impressive the inability of the data assimilation method to approximate DNS results when not using the C_f data combination and $\beta_{cross-diff}$ control. And despite being the best result

obtained, one can say that - even so - they are unsatisfactory when compared to the potential of this technique for other angles.

In view of these two results, the uniqueness of the control acting on the cross-diffusion term is reinforced when compared to the production term. It is evident in the results for $\alpha = 2^\circ$ that the control acting on the production term performs better in several cases; but never in such a way as to be the only viable option for a robust fix. The cross-diffusion term may slightly underperform, but it always gives approximate results.

Given this fact, we propose a more holistic discussion, taking into account all the angles of attack analyzed in this work. For this, only the control parameter in cross-diffusion will be used; together with data for pressure coefficients and skin drag coefficient.

5.3.4 Analysis for Every α

Finally, we propose a complete analysis for all angles of attack; focusing exclusively on the control parameter acting on the cross-diffusion term $\beta_{cross-diff}$ and using the pressure coefficient and the skin drag coefficient as data. Differently from the analysis made in subsection 5.3.2; here we opted for a higher penalization parameter: $\alpha_{pen} = 10^{-8}$. Based on this, and following the same metrics as Table 5.1, we have:

Angle of Attack	Observation	
	C_p	C_f
$\alpha = 0^\circ$	8.54e-3	7.82e-2
$\alpha = 0.5^\circ$	1.04e-2	6.78e-2
$\alpha = 1^\circ$	5.84e-1	1.24e-1
$\alpha = 1.5^\circ$	5.43e-3	1.53e-1
$\alpha = 2^\circ$	2.03e-3	5.64e-2

Table 5.3: Final values for the cost function (black) and the velocity error of the field under the L_2 norm (red) for C_p and C_f with control parameter $\beta_{cross-diff}$ at every angle.

In this table, a direct comparative analysis is made between the results using both data, in such a way that the best result is highlighted in bold. Immediately, one can perceive a relatively balanced division of this comparison, suggesting that there are several intricacies and non-trivial weights in the premise of choosing a data that presents itself as the best source.

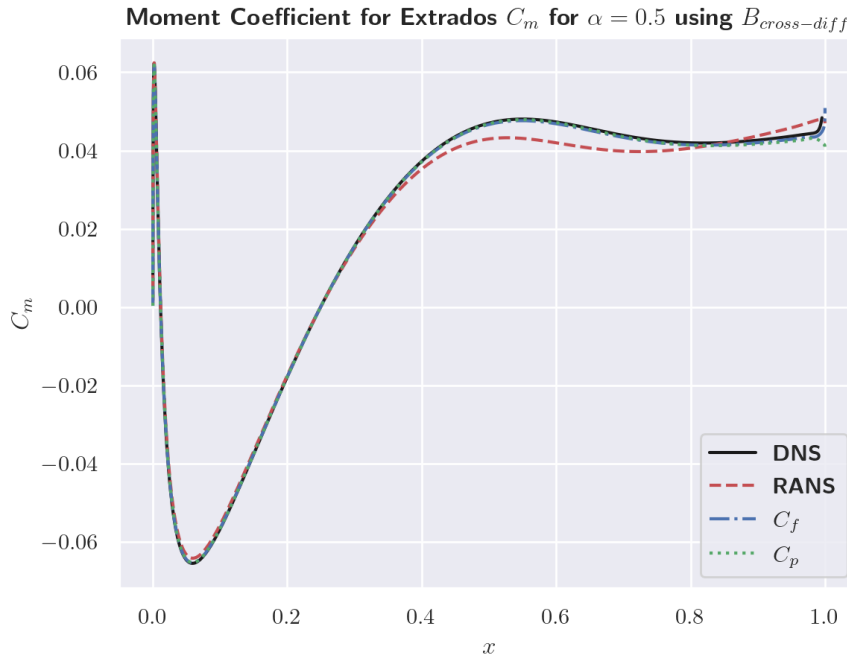


Figure 5.11: Extradorsal moment coefficient at $\alpha = 0.5^\circ$, showing better results when $\beta_{cross-diff}$ is used.

Additionally, for smaller angles such as 0 and 0.5; both results match the DNS results perfectly and do not show any discrepancies, as can be seen in Fig. 5.11

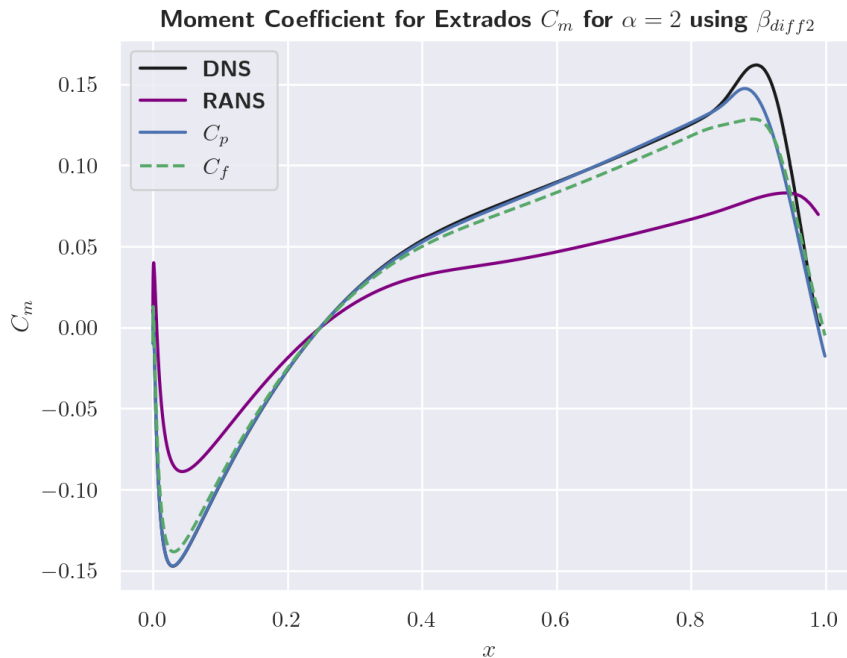


Figure 5.12: Extradorsal moment coefficient at $\alpha = 2^\circ$, showing better results when C_p is used.

However, it is noted that there is a tendency for the skin drag coefficient to present better predictions for the velocity field as a whole. On the other hand, the pressure coefficient performs better

overall in reducing the cost function, thus making it a better candidate for the sole purpose of more accurately predicting aerodynamic forces.

Given these results, it is impossible to choose a data source that can be considered the best. Both have advantages and shortcomings under a holistic analysis, as well as presenting local differences. As discussed earlier, only the combination between C_f and $\beta_{cross-diff}$ presents minimally consistent results for $\alpha = 1^\circ$ (Fig. 5.10b). On the other hand, only C_p more accurately captures some extradorsal efforts at $\alpha = 2^\circ$ (Fig. 5.12).

5.3.5 Broader Strategies

In view of all the discussion presented, one can propose a precious idea, which is presented as the first step to leave the scope of analysis proposed in this subsection. Since there are intrinsic advantages only to the use of the pressure coefficient as a source, and other advantages exclusive to the skin drag coefficient; the performance of an assimilation that takes into account both data simultaneously will be tested.

Unfortunately, this approach does not provide expected results and fails to even provide a sufficient reduction for the cost function, as can be seen in Figure 5.13.

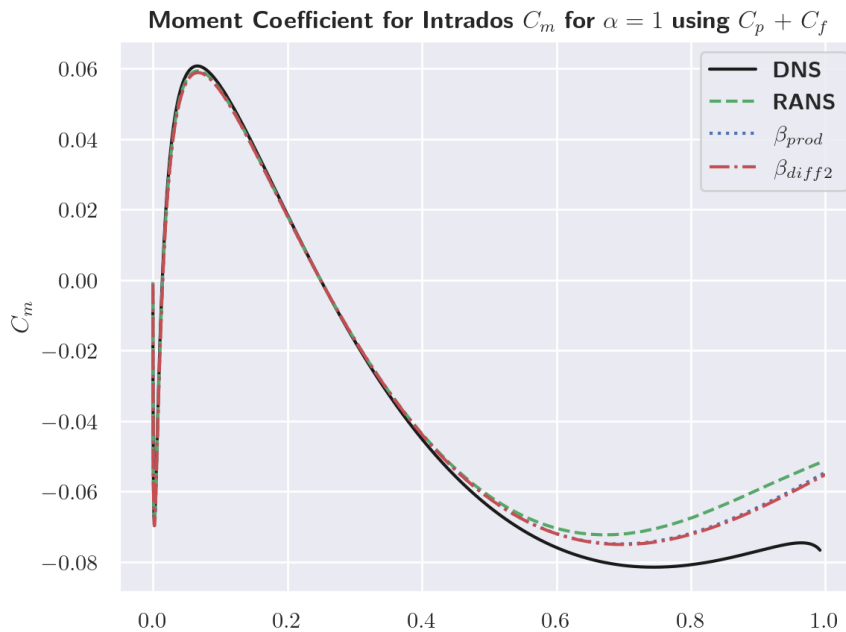


Figure 5.13: Intradorsal moment coefficient at $\alpha = 1^\circ$ using combined parietal data $C_p + C_f$.

However, the discussion presented here does not lose its effect, and possibly one of the only ways to obtain complete results for data assimilation is with the combination of parietal data. This line of thought motivates and leads the research towards other possibilities, now escaping the restrictions initially proposed in this subsection.

5.4 Results: Scenario II

5.4.1 Motivation

Now, taking into account the successes and limitations of an approach based on a relatively inflexible modeling in the face of scarcity of data, we aim to study possibilities that are outside this scope. Therefore, this will be studied in two ways:

- The first is to lift the restriction placed on the exclusive use of parietal data. That is, the results that can be obtained using the entire velocity field will be analyzed. These results will be valuable in order to serve as a comparative case for the success or adversities of using parietal data.
- The second analysis remains within the proposal of using parietal data, more specifically, the combined use of C_p with C_f . However, we will now try to give greater flexibility and correctability to the model through a control parameter that acts as an additional force in the turbulence equation. This parameter will be multiplied only by the modified eddy-viscosity, in order to minimally confer a physical character to the additional term.

5.4.2 Field Data

Immediately, we present the results obtained using field data UV for the previously analyzed case of $\alpha = 2^\circ$. In the Table below the results of Table 5.1 are shown again, in order to facilitate the comparison of results for this case.

Observation	Control Parameter	
	β_{prod}	$\beta_{cross-diff}$
Field Data	9.25e-2 4.51e-2	2.70e-2 1.76e-2
Pressure Coefficient	1.95e-3 7.32e-2	3.41e-3 7.60e-2
Skin Friction Coefficient	3.87e-2 3.87e-2	7.43e-2 7.43e-2

Table 5.4: Final values for the cost function (black) and the velocity error of the field under the L_2 norm (red) using field data, and some previous results, at $\alpha = 2^\circ$.

Unlike the comparisons made in the previous subsection, the analysis of the reduction of the cost function provides few insights into the accuracy of the results, since it does not immediately reflect the behavior of aerodynamic efforts. For this, we can analyze the 5.14, which shows satisfactory results, but entirely comparable with the results using parietal data.

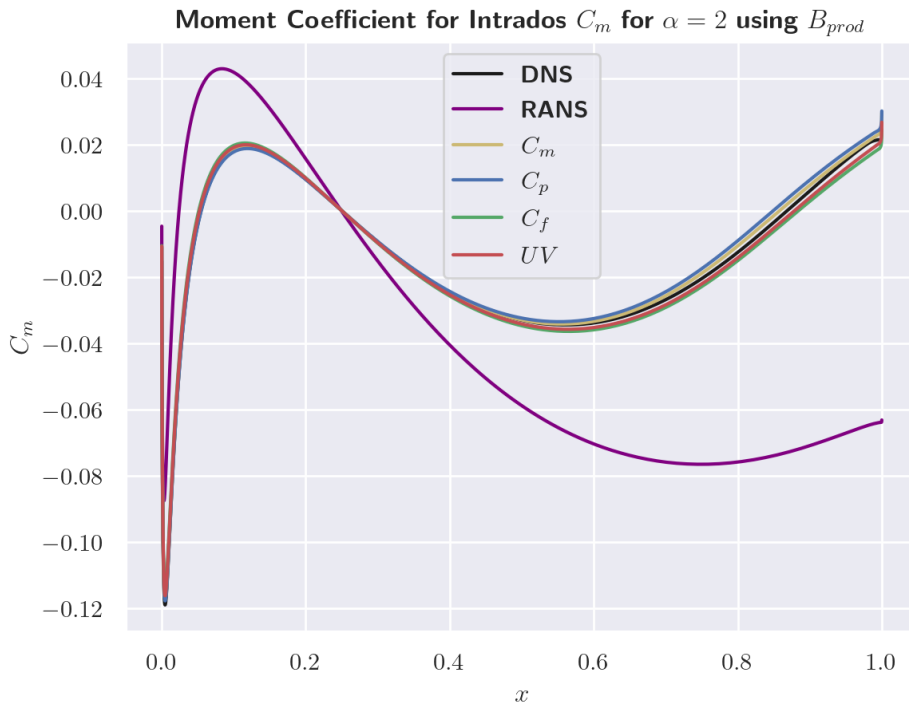


Figure 5.14: Intradosal moment coefficient at $\alpha = 2^\circ$ comparing parietal data and full field data results.

The great advantage of this approach is shown when a direct comparison of the difference between assimilated velocity and DNS velocity is observed; as can be seen in 5.15, in contrast to 5.16.

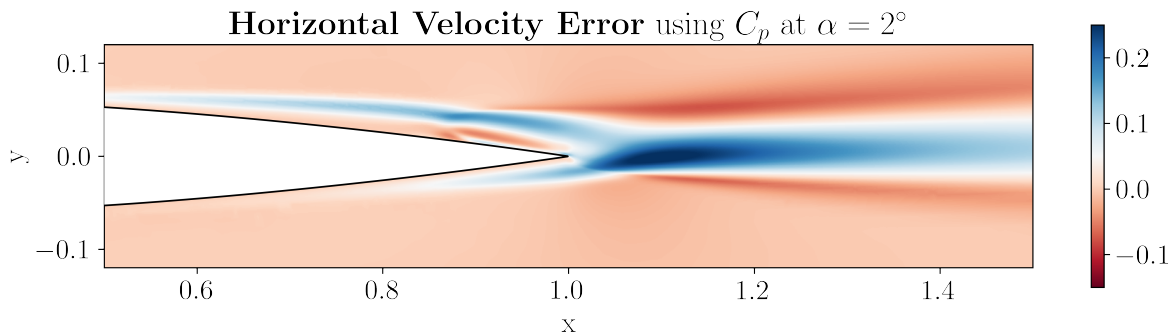


Figure 5.15: Direct subtraction of DNS and assimilated results using parietal data C_p for the horizontal velocity at $\alpha = 2^\circ$.

From a critical point of view, it can be concluded that the use of field data is justified and valuable when the discrepancy between the real phenomenon and the uncorrected result is more spatially distributed. As an example, one can cite the work of Volpiani et al. [39], in which the correction fills a large part of the observed flow. As for the study of laminar separation flutter, the main differences are noticed mainly in the upper part of the trailing edge; where there is the LSB.

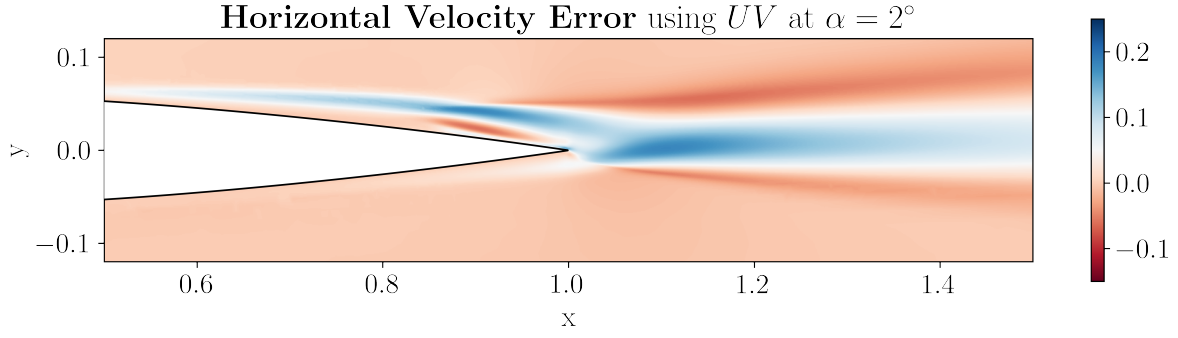


Figure 5.16: Direct subtraction of DNS and assimilated results using full field data UV for the horizontal velocity at $\alpha = 2^\circ$.

Therefore, since the phenomenon studied is dominated by a dynamic that occurs in a relatively concentrated region, the full-field correction proves to be functional, however, ineffective for capturing the details linked to the laminar separation flutter.

5.4.3 Additional Forcing

Since the idea of using field data did not bring significant improvements, we will now try an alternative to the multiplicative control parameter; maintaining parietal data. More specifically, the combination of pressure coefficient and skin friction coefficient data will be used to correct an additional force.

Unlike the work by Franceschini et al. [5], this additional term will be multiplied by the modified turbulent viscosity. This choice is justified by the adjoint analysis of the modified eddy-viscosity. One should recall that this quantity is the result of the gradient of the cost function with respect to the additional forcing by itself (Eq. 5.9).

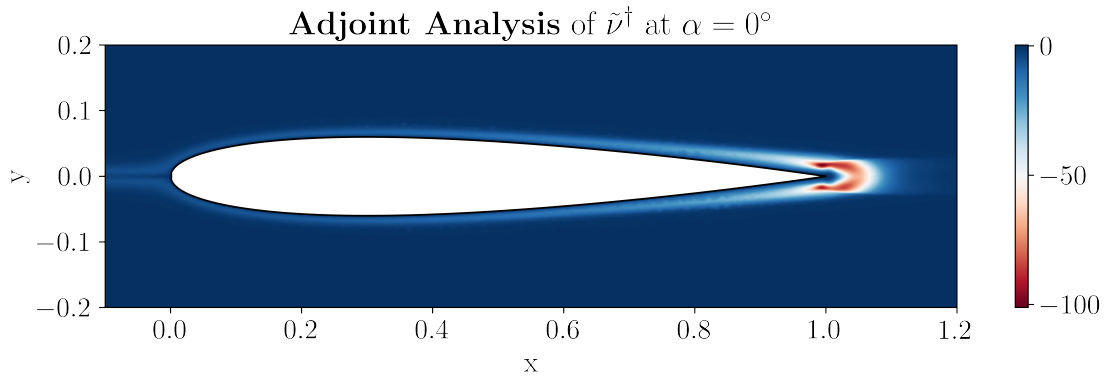


Figure 5.17: Adjoint analysis of \tilde{v}^\dagger at $\alpha = 0^\circ$.

Figure 5.17 shows that, despite the magnitude, this property is not null for regions in which the flow is still laminar. Notably, this can be seen really close to the airfoil for regions at $x < 0.6$. This means that using the additional forcing in Franceschini's framework is susceptible to correct areas where the turbulence model should be strictly off. This mathematical and physical inconsistency can be easily corrected by multiplying the additional forcing by the modified eddy-viscosity:

$$\bar{\mathbf{u}} \cdot \nabla \tilde{v} = s(\tilde{v}, \nabla \tilde{v}, \nabla \bar{\mathbf{u}}) + \tilde{f}_{\tilde{v}} \tilde{v}$$

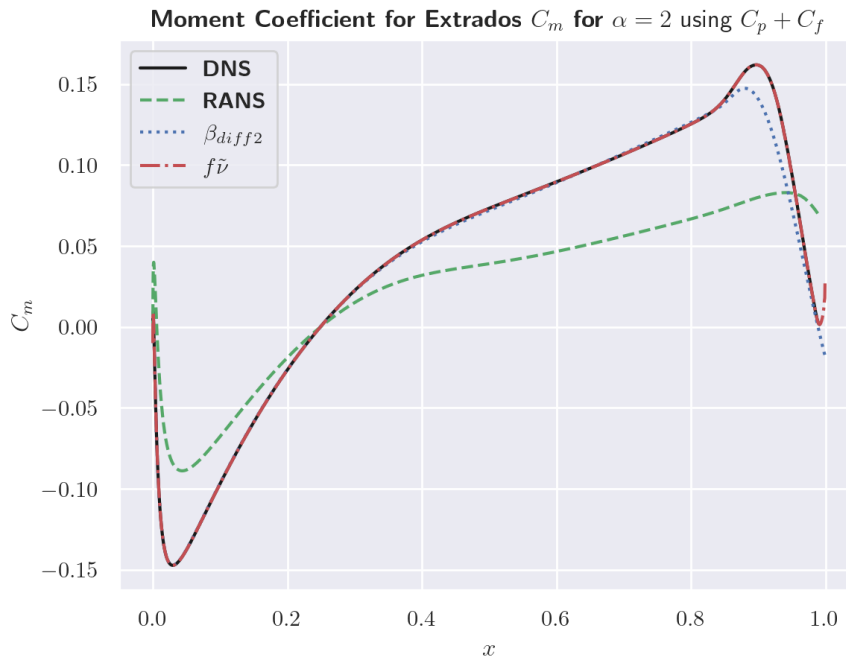


Figure 5.18: Extradorsal moment coefficient at $\alpha = 2^\circ$ using combined parietal data and an additional forcing.

And therefore, the model now is physically consistent regarding the spacial domain in which it can boost or diminish turbulent behavior.

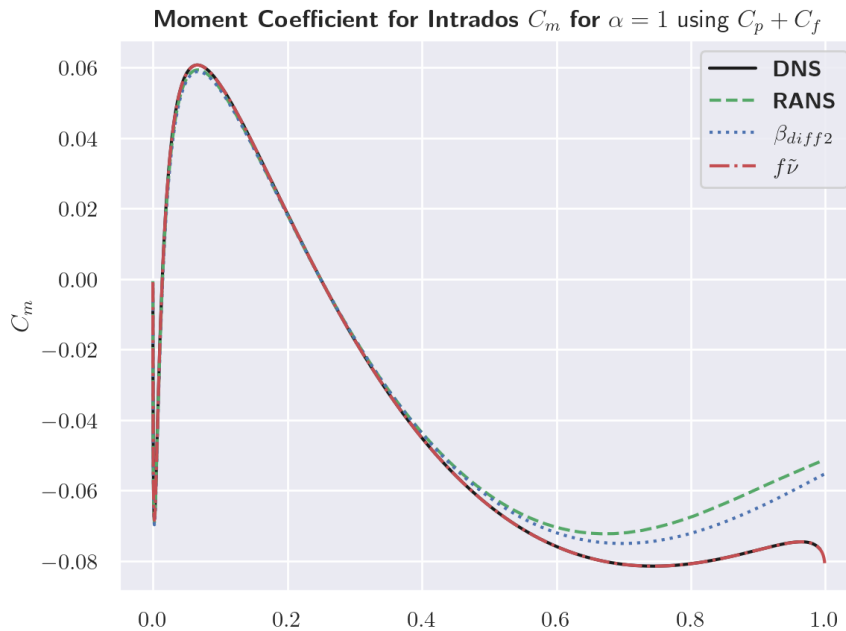


Figure 5.19: Intradorsal moment coefficient at $\alpha = 1^\circ$ using combined parietal data and an additional forcing.

As it can be seen, when analyzing the cases that presented more inconsistencies ($\alpha = 2$ for ex-

tradorsal C_m and $\alpha = 2$ for intradorsal C_m), we noticed a complete agreement with the DNS data. And in fact, through this technique, all aerodynamic effort curves consistently show perfect agreement with DNS data.

Given this, it can be said that removing the restriction imposed on the exclusive use of multiplicative control parameters is highly justifiable. We also reinforce that for this approach it was not necessary to leave the parietal data frame. This is of absolute importance as it denotes that perfectly accurate results can be obtained using a limited and localized amount of data.

5.5 Conclusion

In a quick review of this chapter, we present the mathematical formalism associated with the Data Assimilation method using RANS-SA modeling, with a transition model. One can say that the originality of this study is associated with the comparative character of several choices that are commonly made without a robust physical and mathematical discussion.

First, it is necessary to take into account the high-fidelity data that will be used for the assimilation (which many studies readily make use of full-field data). The study carried out here shows that, indeed, for a more accurate description of the velocity field in its smallest details, field data are indispensable. However, the phenomenon studied here is partially linked to structural efforts; which enriches the potential of description linked to the parietal data of this structure. In the analyzes carried out in subsection 5.3 and 5.4, this fact becomes evident. The use of aerodynamic coefficients (C_p , C_f , C_m) is not only sufficient for an accurate description of the phenomenon, it is also more powerful than the use of whole field data; notably, when using combined parietal data ($C_p + C_f$).

Parallel to this, there is the choice of the ideal control parameter for the modeling - either by a multiplicative coefficient in the original terms of Spalart-Allmaras model, or an additional forcing to the equation. In this line of studies, several results were complemented by sensitivity analyzes of the cost function with respect to these control parameters. Given this, we show that the term of destruction are unable to correctly describe the dynamics of the phenomenon. Furthermore, the production and cross-diffusion terms present robust results; as discussed in subsection 5.3. However, we have shown that only with the addition of forcing multiplied by the modified turbulent viscosity we get results that perfectly resemble the high fidelity data.

These results can be easily extended to a critique of the physical validity of the Spalart-Allmaras model for the phenomenon studied. Even correcting locally the different physical effects that are contemplated by the model (production, diffusion and destruction of turbulence in the way they were formulated); we have not achieved a perfect description. Only when we subtly leave the framework of hypotheses that underlie the model, do we obtain the expected agreement.

Conclusion

In a general review of the issues and results addressed by this work, there is a focus on a comparative analysis of turbulence models corrected by the data assimilation procedure. At first, the nature of the phenomenon of laminar separation flutter and its intricacies was established; mainly its localized character and its effect on aerodynamic efforts. Then, high-fidelity data were presented and discussed, which served as a basis for data driven modeling. Consecutively, the mathematical and numerical frameworks were fully addressed; in addition to a reiteration of the inability of classical methods to accurately predict aerodynamic forces. Finally, the different corrections made possible by the VDA were presented, critically discussed and their results analyzed.

Among the main results and discussions, the advantages and shortcomings of using parietal data over full field data are reiterated. The latter, despite providing more details on the physical dynamics of the phenomenon, is not justified as an ideal data for the assimilation procedure. When analyzing only the performance of the prediction of aerodynamic efforts, the parietal data are excellent; which is convenient, given their abundance in different works and the ease of obtaining them experimentally.

From a comparative point of view of the different types of parietal data, we find that there are predictions that undoubtedly occur better with certain choices; such as using the skin friction coefficient for $\alpha = 1^\circ$ and using the pressure coefficient for $\alpha = 2^\circ$. This fact directed the work to explore the combined use of these data, enabling the assimilated model to provide both dynamics, giving compelling results.

Finally, models based on corrective parameters and additional forcings were also compared. Despite the physical understanding favored within the framework of multiplicative parameters, the additional forcing allows a superposition of physical corrections that proves to be more complete and effective in the prediction of aerodynamic efforts. It also reinforces the justifications used throughout the work that made use of analyzes from the adjunct field; leading up to an improvement of the classically found model of additional forcing.

Among the perspectives and possible directions that this research can take, it is impossible not to mention the generalization potential of these corrected models within the FIML (Field Inversion Machine Learning) paradigm. In this way, neural networks or decision trees can be used to predict corrective control parameters; thus supporting a turbulence model corrected by machine learning. This paradigm is of extreme interest as it will allow the generalization of the corrected model with data assimilation to subtly different configurations for which there is no high fidelity data.

Such an approach, however, requires a careful analysis of the input features that will be used for the model training stage; in addition to the architectural choices of the neural network. This area blends classical knowledge of fluid mechanics with an understanding of which physical properties best contribute and describe the corrective parameter.

Bibliography

- [1] D Poirel, Y Harris, and A Benaïssa. Self-sustained aeroelastic oscillations of a naca0012 airfoil at low-to-moderate reynolds numbers. *Journal of Fluids and Structures*, 24(5):700–719, 2008.
- [2] Diogo Sabino. *Aeroelastic instabilities of an airfoil in transitional flow regimes*. PhD thesis, Université de Toulouse, 2022.
- [3] Philippe Spalart and Steven Allmaras. A one-equation turbulence model for aerodynamic flows. In *30th aerospace sciences meeting and exhibit*, page 439, 1992.
- [4] Karthik Duraisamy, Gianluca Iaccarino, and Heng Xiao. Turbulence modeling in the age of data. *arXiv preprint arXiv:1804.00183*, 2018.
- [5] Lucas Franceschini, Denis Sipp, and Olivier Marquet. Mean-flow data assimilation based on minimal correction of turbulence models: Application to turbulent high reynolds number backward-facing step. *Physical Review Fluids*, 5(9):094603, 2020.
- [6] H Glauert. The force and moment on an oscillating aerofoil. In *Vorträge aus dem Gebiete der Aerodynamik und verwandter Gebiete*, pages 88–95. Springer, 1930.
- [7] Th H von Karman and William R Sears. Airfoil theory for non-uniform motion. *Journal of the Aeronautical Sciences*, 5(10):379–390, 1938.
- [8] A Ro Collar. The expanding domain of aeroelasticity. *The Aeronautical Journal*, 50(428):613–636, 1946.
- [9] Denis Busquet. *Study of a high Reynolds number flow around a two dimensional airfoil at stall; an approach coupling a RANS framework and bifurcation theory*. PhD thesis, Institut polytechnique de Paris, 2020.
- [10] PR Owen and L Klanfer. On the laminar boundary layer separation from the leading edge of a thin aerofoilv. Technical report, Aeronautical Research Council London (United Kingdom), 1953.
- [11] Tianyu Xia, Hao Dong, Liming Yang, Shicheng Liu, and Zhou Jin. Investigation on flow structure and aerodynamic characteristics over an airfoil at low reynolds number—a review. *AIP Advances*, 11(5):050701, 2021.
- [12] Thomas J Mueller and Stephen M Batill. Experimental studies of separation on a two-dimensional airfoil at low reynolds numbers. *AIAA journal*, 20(4):457–463, 1982.
- [13] Tomohisa Ohtake, Yusuke Nakae, and Tatsuo Motohashi. Nonlinearity of the aerodynamic characteristics of naca0012 aerofoil at low reynolds numbers. *Japan Society of Aeronautical Space Sciences*, 55(644):439–445, 2007.

- [14] Steven A Orszag. Analytical theories of turbulence. *Journal of Fluid Mechanics*, 41(2):363–386, 1970.
- [15] François G Schmitt. About boussinesq’s turbulent viscosity hypothesis: historical remarks and a direct evaluation of its validity. *Comptes Rendus Mécanique*, 335(9-10):617–627, 2007.
- [16] O Reynolds. On the dynamical theory of incompressible viscous fluids and the determination of the criterion (reprinted from papers on mechanical and physical subjects, vol 2, pg 535-577, 1901). In *Proceedings of the Royal Society-Mathematical and Physical Sciences*, volume 451, pages 5–47. ROYAL SOC 6-9 CARLTON HOUSE TERRACE, LONDON SW1Y 5AG, ENGLAND, 1995.
- [17] JCR Hunt. Mathematical models of turbulence. by be launder and db spalding. academic press, 1972. *Journal of Fluid Mechanics*, 57(4):826–828, 1973.
- [18] David C Wilcox. Formulation of the kw turbulence model revisited. *AIAA journal*, 46(11):2823–2838, 2008.
- [19] Georgi Kalitzin, Gorazd Medic, Gianluca Iaccarino, and Paul Durbin. Near-wall behavior of rans turbulence models and implications for wall functions. *Journal of Computational Physics*, 204(1):265–291, 2005.
- [20] Florian R Menter, R Langtry, and S Völker. Transition modelling for general purpose cfd codes. *Flow, turbulence and combustion*, 77(1):277–303, 2006.
- [21] Samet C Cakmakcioglu, Onur Bas, Riccardo Mura, and Unver Kaynak. A revised one-equation transitional model for external aerodynamics. In *AIAA Aviation 2020 Forum*, page 2706, 2020.
- [22] Stefan Bergman. *Contributions to the theory of partial differential equations*. Number 33. Princeton University Press, 1955.
- [23] John M Lewis, Sivaramakrishnan Lakshminarayanan, and Sudarshan Dhall. *Dynamic data assimilation: a least squares approach*, volume 13. Cambridge University Press, 2006.
- [24] Geir Evensen et al. *Data assimilation: the ensemble Kalman filter*, volume 2. Springer, 2009.
- [25] Alejandro Gronska, Dominique Heitz, and Etienne Mémin. Inflow and initial conditions for direct numerical simulation based on adjoint data assimilation. *Journal of Computational Physics*, 242:480–497, 2013.
- [26] Hiroshi Kato and Shigeru Obayashi. Approach for uncertainty of turbulence modeling based on data assimilation technique. *Computers & Fluids*, 85:2–7, 2013.
- [27] Vincent Mons, J-C Chassaing, Thomas Gomez, and Pierre Sagaut. Reconstruction of unsteady viscous flows using data assimilation schemes. *Journal of Computational Physics*, 316:255–280, 2016.
- [28] Rudolph Emil Kalman. A new approach to linear filtering and prediction problems. 1960.
- [29] Takao Suzuki. Reduced-order kalman-filtered hybrid simulation combining particle tracking velocimetry and direct numerical simulation. *Journal of Fluid Mechanics*, 709:249–288, 2012.
- [30] CH Colburn, JB Cessna, and TR Bewley. State estimation in wall-bounded flow systems. part 3. the ensemble kalman filter. *Journal of Fluid Mechanics*, 682:289–303, 2011.

- [31] Dominique Heitz, Etienne Mémin, and Christoph Schnörr. Variational fluid flow measurements from image sequences: synopsis and perspectives. *Experiments in fluids*, 48(3):369–393, 2010.
- [32] Yin Yang, Cordelia Robinson, Dominique Heitz, and Etienne Mémin. Enhanced ensemble-based 4dvar scheme for data assimilation. *Computers & Fluids*, 115:201–210, 2015.
- [33] François-Xavier Le Dimet and Olivier Talagrand. Variational algorithms for analysis and assimilation of meteorological observations: theoretical aspects. *Tellus A: Dynamic Meteorology and Oceanography*, 38(2):97–110, 1986.
- [34] Dimitry PG Foures, Nicolas Dovetta, Denis Sipp, and Peter J Schmid. A data-assimilation method for reynolds-averaged navier–stokes-driven mean flow reconstruction. *Journal of fluid mechanics*, 759:404–431, 2014.
- [35] Sean Symon, Nicolas Dovetta, Beverley J McKeon, Denis Sipp, and Peter J Schmid. Data assimilation of mean velocity from 2d piv measurements of flow over an idealized airfoil. *Experiments in fluids*, 58(5):1–17, 2017.
- [36] Marco A Iglesias, Kody JH Law, and Andrew M Stuart. Ensemble kalman methods for inverse problems. *Inverse Problems*, 29(4):045001, 2013.
- [37] Zhiyong Li, Huaibao Zhang, Sean CC Bailey, Jesse B Hoagg, and Alexandre Martin. A data-driven adaptive reynolds-averaged navier–stokes $k-\omega$ model for turbulent flow. *Journal of Computational Physics*, 345:111–131, 2017.
- [38] Roger Fletcher. *Practical methods of optimization*. John Wiley & Sons, 2013.
- [39] Pedro Stefanin Volpiani, Morten Meyer, Lucas Franceschini, Julien Dandois, Florent Renac, Emeric Martin, Olivier Marquet, and Denis Sipp. Machine learning-augmented turbulence modeling for rans simulations of massively separated flows. *Physical Review Fluids*, 6(6):064607, 2021.

List of Tables

5.1	Final values for the cost function (black) and the velocity error of the field under the L_2 norm (red) for every observation and control parameter at $\alpha = 2^\circ$, using $\alpha_{pen} = 10^{-7}$.	41
5.2	Final values for the cost function at $\alpha = 1^\circ$.	44
5.3	Final values for the cost function (black) and the velocity error of the field under the L_2 norm (red) for C_p and C_f with control parameter $\beta_{cross-diff}$ at every angle.	45
5.4	Final values for the cost function (black) and the velocity error of the field under the L_2 norm (red) using field data, and some previous results, at $\alpha = 2^\circ$.	48

List of Figures

1.1	Static instability and dynamic instability, respectively. Sabino et al. [2]	10
1.2	Schematic illustration of a two-dimensional laminar boundary layer separation and of a laminar separation bubble, respectively. Busquet et al. [9]	11
1.3	A short laminar separation bubble and a long laminar separation bubble, respectively. Xia et al. [11]	11
1.4	On the left, evolution of the time-averaged drag coefficient with the angle of attack for different Reynolds numbers, from the experiments of Ohtake et al. [13]. On the right, evolution of the time-averaged lift coefficient with the angle of attack for $Re = 130000$, from the experiments of Mueller et al. [12]	12
2.1	Horizontal velocity comparison angle of attack $\alpha = 0^\circ$	14
2.2	Horizontal velocity comparison angle of attack $\alpha = 2^\circ$	15
2.3	Horizontal velocity for $\alpha = 2^\circ$, denoting the Laminar Separation Bubble.	15
2.4	Fluctuation term in z direction comparison for different angles.	16
2.5	Boussinesq validity analysis for different angles of attack.	17
2.6	Turbulence production for different angles of attack.	18
2.7	Global aerodynamic efforts for different angles of attack	19
2.8	Skin Friction Coefficient at extrados for $\alpha = 2^\circ$	19
3.1	Eddy-viscosity ν_t and modified eddy-viscosity $\tilde{\nu}$. [19]	23
4.1	Schematic illustration of the computational domain for the simulation. Sabino et al. [2]	27
4.2	Two-dimensional triangular mesh around the NACA0012 airfoil, at $\alpha = 0^\circ$, on the top left, with the close-up views near the airfoil, on the bottom left, and near the leading and trailing edge zones, on the right. Sabino et al. [2]	29
4.3	Two- and three-dimensional standard element cells: illustration of the number of degrees of freedom for the P_1 and P_2 finite element spaces. Sabino et al. [2]	29
4.5	Direct subtraction of DNS and RANS-SA results for the horizontal velocity at $\alpha = 1^\circ$	31
4.6	Direct subtraction of DNS and RANS-SA results for the horizontal velocity at $\alpha = 2^\circ$	31
5.1	Sketch of the BFGS algorithm for a general problem, having \mathbf{f} as a control parameter and \mathbf{q} as state. The adjoint variable is denoted by \mathbf{q}^\dagger . Franceschini et al. [5]	37
5.2	Sensibility analysis using parietal data C_f at $\alpha = 2^\circ$	38
5.3	Sensibility analysis using parietal data C_m at $\alpha = 2^\circ$	39
5.4	Sensibility analysis using full field data UV at $\alpha = 2^\circ$	39
5.5	L-curve analysis for assimilations performed using C_f parietal data for the correction of the production term β_{prod} ; at $\alpha = 2^\circ$	40
5.6	Sensitivity Analysis with respect to the control parameter acting on the destruction term.	42

5.7 Sensitivity Analysis with respect to the control parameter acting on the production term. 42

5.8 Complete comparison of control parameters for the description of the extradorsal moment coefficient using C_p at $\alpha = 2^\circ$ 43

5.11 Extradorsal moment coefficient at $\alpha = 0.5^\circ$, showing better results when $\beta_{cross-diff}$ is used. 46

5.12 Extradorsal moment coefficient at $\alpha = 2^\circ$, showing better results when C_p is used. 46

5.13 Intradorsal moment coefficient at $\alpha = 1^\circ$ using combined parietal data $C_p + C_f$ 47

5.14 Intradorsal moment coefficient at $\alpha = 2^\circ$ comparing parietal data and full field data results. 49

5.15 Direct subtraction of DNS and assimilated results using parietal data C_p for the horizontal velocity at $\alpha = 2^\circ$ 49

5.16 Direct subtraction of DNS and assimilated results using full field data UV for the horizontal velocity at $\alpha = 2^\circ$ 50

5.17 Adjoint analysis of \tilde{v}^\dagger at $\alpha = 0^\circ$ 50

5.18 Extradorsal moment coefficient at $\alpha = 2^\circ$ using combined parietal data and an additional forcing. 51

5.19 Intradorsal moment coefficient at $\alpha = 1^\circ$ using combined parietal data and an additional forcing. 51